Identifying physics beyond SMEFT in the angular distribution of $\Lambda_b \to \Lambda_c(\to \Lambda\pi)\tau\bar{\nu}_\tau$ decay

Siddhartha Karmakar,* Susobhan Chattopadhyay,† and Amol Dighe‡
Tata Institute of Fundamental Research, Homi Bhabha Road, Colaba, Mumbai 400005, India

(Received 1 November 2023; accepted 2 June 2024; published 8 July 2024)

In the Standard Model effective field theory (SMEFT), the $SU(2)_L \times U(1)_Y$ symmetry of the Standard Model is linearly realized. However, it is possible that more general effective field theories, such as the Higgs effective field theory (HEFT) where this symmetry is realized nonlinearly, are needed to describe the data. Identifying physics beyond SMEFT could shed light on the nature of Higgs and the realization of the electroweak symmetry. We explore the possibility of such an identification by studying the effects of scalar and vector new physics operators on the angular distribution of $\Lambda_b \to \Lambda_c(\to \Lambda\pi)\tau\bar{\nu}_\tau$. This decay is sensitive to the six-dimensional effective operator $O_V^{LR} \equiv (\bar{\tau}\gamma^\mu P_L \nu_\tau)(\bar{c}\gamma_\mu P_R b)$, which is present in HEFT but suppressed in SMEFT. We identify the angular observables that can have significant contributions from O_V^{LR} and hence would be useful for probing not only beyond the Standard Model physics but also physics beyond SMEFT. We further find that constraining the branching ratio of $B_c \to \tau\bar{\nu}_\tau$ would be crucial for performing this task.

DOI: 10.1103/PhysRevD.110.015010

I. INTRODUCTION

The Standard Model (SM) of particle physics describes the properties of known matter and forces to a great accuracy. However, there are reasons to believe that the SM is not complete. Certain phenomena such as the baryon asymmetry in the Universe, neutrino oscillations, and the existence of dark matter are not explained in the SM. This indicates that there exists new physics (NP) beyond SM. One way this NP can be probed in direct searches is by producing new particles in high-energy particle colliders. In a complementary approach, the effects of NP can be identified indirectly with the help of precision measurements in relatively low-energy processes.

While the effect of NP can be searched for in specific models, the effective field theory (EFT) techniques provide a model-independent and common framework to perform more general analyses, whose results can be translated into broad classes of scenarios beyond the Standard Model (BSM). In the field of flavor physics, EFT methods are employed to analyze the effect of NP with the help of precision measurements.

*Contact author: siddhartha@theory.tifr.res.in
†Contact author: susobhan.chattopadhyay@tifr.res.in
‡Contact author: amol@theory.tifr.res.in

In the modern view, the SM is considered as the leading part of an EFT that respects the SM symmetry group $SU(3)_C \times SU(2)_L \times U(1)_Y$. In this view, the SM is expected to be valid up to an NP scale Λ, above which additional dynamical degrees of freedom appear. The effects of NP can be encoded in higher-dimensional operators that are suppressed by powers of the NP scale Λ,

$$\mathcal{L} = \mathcal{L}_{\rm SM} + \frac{1}{\Lambda} C^{(5)} O^{(5)} + \frac{1}{\Lambda^2} \sum_i C_i^{(6)} O_i^{(6)} + \mathcal{O}\left(\frac{1}{\Lambda^3}\right). \quad (1)$$

The above equation describes the Standard Model effective field theory (SMEFT) [1–4] when all the operators $O_i^{(d)}$ are composed of only SM fields and respect the SM symmetry group. Here d denotes the dimensionality of the operator $O_i^{(d)}$. The NP contributions are parametrized in terms of the Wilson coefficients $C_i^{(d)}$.

In SM, the Higgs boson (h) and the three Goldstone bosons (ϕ_1, ϕ_2, ϕ_3) are parts of a single $SU(2)_L$ doublet field H. This embedding is referred to as a linear realization of the electroweak (EW) symmetry [5]. This feature is maintained in SMEFT. At present, the measurements of production and decay channels of the Higgs boson at the LHC are consistent with the SM Higgs mechanism of EW symmetry breaking and hence with SMEFT [6]. However, in BSM scenarios, the four fields $(h, \phi_1, \phi_2, \phi_3)$ need not be embedded into a single doublet H. Such scenarios cannot be described in SMEFT, and searching for these

scenarios is equivalent to probing the mechanism of EW symmetry breaking.

Possible deviations of couplings of the Higgs boson from the SM prediction would indicate the need for a more general extension of SM, even beyond SMEFT. Note that the measured values of the Higgs boson couplings to gauge bosons and top quark are compatible with the SM to about $\mathcal{O}(10\%)$ [7–9]. However, for the Higgs boson couplings to other quarks and leptons, or for the triple-Higgs boson coupling, larger deviations are possible [7–9]. For example, in the Higgs effective field theory (HEFT) [10–12], one can have modified interactions of the Higgs boson while keeping its gauge interactions unchanged. Here the Higgs sector consists of a singlet $\hat{h}$ boson that is invariant under the EW symmetry and three Goldstone fields $(\hat{\phi}_1, \hat{\phi}_2, \hat{\phi}_3)$ that transform nonlinearly under this symmetry [5]. Thus, the $SU(2)_L \times U(1)_Y$ symmetry is realized nonlinearly in HEFT, and the manifest gauge symmetry in HEFT is only $SU(3)_C \times U(1)_Q$. Therefore, HEFT is a more general effective theory than SMEFT, i.e., HEFT $\supset$ SMEFT $\supset$ SM [13]. In particular, many HEFT operators at a given dimension may not appear in SMEFT at the same dimension, though they may appear at higher dimensions and therefore would typically be suppressed.

Searches for beyond-SMEFT physics in ATLAS and CMS focus on the precise measurements of Higgs couplings with fermions and gauge bosons [7]. A complementary approach to extract evidence for nonlinearly realized EW symmetry is via flavor physics, which offers indirect probes of heavy new physics that are complementary to direct collider searches. Many of the recently observed anomalies in B meson decays, e.g., $R(D^{(*)})$ [14–17] and $R(J/\psi)$ [18] that correspond to the charged-current transition $b \to c\tau\nu_\tau$, and $\mathcal{B}(B^+ \to K^+\mu^+\mu^-)$ [19], $\mathcal{B}(B^+ \to K^+e^+e^-)$ [20], and P_5' [21–23] that correspond to the neutral-current transitions $b \to sll$, indicate the possibility of BSM physics. While there are viable solutions to these anomalies within SMEFT, the question of whether these anomalies arise from physics beyond SMEFT is still open.

For flavor physics processes, the relevant energy scale is around the mass of the b quark. At this energy scale, the heavier SM particles $(W^\pm, Z^0, h, t)$ are no longer the degrees of freedom and are integrated out. The resultant EFT is called the low-energy effective field theory (LEFT),[1] [28] in which the effective Lagrangian is

$$\mathcal{L}_{\text{LEFT}} = \mathcal{L}_{\text{SM}} + \sum_{d\geq 5} \sum_i (G_F)^{\frac{d}{2}-2} C_i^{(d)} \mathcal{O}_i^{(d)}. \tag{2}$$

Here, the expansion is in terms of the Fermi constant $G_F = (\sqrt{2} g_W^2)/(8M_W^2)$. The operators are written in terms of the dynamical fields below the EW symmetry-breaking scale. Thus, LEFT is an $SU(3)_C \times U(1)_Q$ invariant effective theory valid below the EW scale.

The information about how the $SU(2)_L \times U(1)_Y$ symmetry is realized above the EW scale can be extracted by matching the LEFT operators to EFTs valid beyond the electroweak scale, such as SMEFT or HEFT. Most of the dimension-six operators do not require any source of electroweak symmetry breaking beyond the SM and these operators can be directly mapped onto six-dimensional SMEFT and HEFT operators [24,29,30]. However, there are some dimension-six LEFT operators that cannot be generated from dimension-six SMEFT operators but can be generated from HEFT at this order [31–33]. There exist NP models where certain dimension-six operators are generated but cannot be mapped to SMEFT at the leading order—for example, the nonstandard Higgs model with a strongly coupled scalar [32] and the model with a W' that couples to right-handed quarks and left-handed leptons [34]. Further discussions on models requiring a framework beyond SMEFT can be found in [35], where a new class of BSM states called "Loryons" is proposed. Loryons are NP particles whose physical mass is dominated by a contribution from the vacuum expectation value of the Higgs boson. However, the effect of integrating out such fields cannot be incorporated into SMEFT and would require an EFT framework where the EW symmetry is nonlinearly realized. The study of such operators will allow us to identify new physics beyond SMEFT.

One such LEFT operator is $O_V^{LR} \equiv (\bar{\tau}\gamma^\mu P_L \nu)(\bar{c}\gamma_\mu P_R b)$ [32,33,36], which corresponds to the quark-level transition $b \to c\tau\nu_\tau$. This operator can be generated at the leading order from the HEFT operator $\mathcal{O}_{FY11} = (\bar{l}UP_- r)(\bar{r}P_+ U^\dagger l)$ [36]. There is no SMEFT operator that can directly yield such a flavor nonuniversal O_V^{LR} at the low scale. The SMEFT dimension-six operator $O_{Hud} = (H^\dagger i\overleftrightarrow{D}_\mu H)(\bar{u}\gamma^\mu d)$ induces an anomalous $b - c - W$ coupling and contributes to O_V^{LR} [29,37], but here the W coupling to the leptons is flavor universal and would not contribute to the $b \to c\tau\nu_\tau$ anomalies. To generate the operator O_V^{LR} only in the τ sector, we need the dimension-eight SMEFT operator $O_{l^2udH^2} = (\bar{l}dH)(\tilde{H}^\dagger \bar{u} l)$, whose coefficient would be suppressed by an extra factor of v^2/Λ^2. For this reason, O_V^{LR} is neglected in many EFT analyzes based on SMEFT (e.g., [38–42]). However, in the context of mesons, fits to data on $R(D^{(*)})$, $R(J/\psi)$, and $\mathcal{B}(B_c \to \tau^+\nu)$ have indicated that significant contributions from this operator are possible [33,43,44].

A potential baryonic process involving $b \to c\tau\nu_\tau$, which could also offer avenues of probing O_V^{LR}, is the decay $\Lambda_b \to \Lambda_c \tau\bar{\nu}_\tau$. The baryons Λ_b and Λ_c are spin-half particles. As a result, all the vector and the scalar effective operators affect $\Lambda_b \to \Lambda_c \tau\bar{\nu}_\tau$ decay. In contrast, for the mesonic mode $B \to D$, the axial vector, and the pseudoscalar operators do not contribute at the leading order, and

[1]LEFT is sometimes referred to as weak effective field theory (WET or WEFT) in literature [24–27].

for $B \to D^*$, the scalar operator does not contribute at the leading order [45]. Furthermore, the form factors in the baryonic mode are different from those in the mesonic modes. Thus, the baryonic mode offers observables complementary to those in the mesonic modes to study the new physics effects. The large production cross section of Λ_b at LHC and the well-known form factors for $\Lambda_b \to \Lambda_c$ make this baryonic decay mode a good candidate to complement its mesonic counterpart. Recently, the first observation of this process was reported at LHCb with a significance of 6.1σ [46]. The angular distribution of final state particles in $\Lambda_b \to \Lambda_c \tau \bar{\nu}_\tau$ process [41,47–53] and further in $\Lambda_b \to \Lambda_c(\to \Lambda\pi)\tau\bar{\nu}_\tau$ process [40,42,45,54–56] offers multiple observables and ratios of observables where some of the systematic and hadronic uncertainties would cancel. We identify the coefficients of terms in this angular distribution and their ratios, which would be sensitive to O_V^{LR}. We also point out those observables that can show distinct signatures of the O_V^{LR} contribution.

In Sec. II, we present the angular distribution of $\Lambda_b \to \Lambda_c(\to \Lambda\pi)\tau\bar{\nu}_\tau$ decay in terms of the three physical angles involved therein. We calculate angular observables in terms of helicity amplitudes. The efficiencies of these angular observables for identifying the effects of O_V^{LR} are analyzed in Sec. III. We present our concluding remarks in Sec. IV. Appendix B provides the weighting functions that can be used to extract the angular observables using the method of angular moments. Appendix C maps our expressions for angular distribution with earlier literature in order to clarify the notation. In Appendix D, we show a comparison between the effectiveness of the angular observables in different q^2 bins for identifying the effects of O_V^{LR} with two possible upper bounds on $\mathcal{B}(B_c \to \tau\bar{\nu}_\tau)$.

II. ANGULAR DISTRIBUTION OF $\Lambda_b \to \Lambda_c(\Lambda\pi)\tau\bar{\nu}_\tau$ DECAY

In the language of LEFT, the effective Hamiltonian for the quark-level transition $b \to c\tau\bar{\nu}_\tau$ may be written as [40,57]

$$\mathcal{H}_{\rm eff} = \frac{4G_F V_{cb}}{\sqrt{2}}[(1+g_L)\mathcal{O}_V^{LL} + g_R\mathcal{O}_V^{LR} + g_S\mathcal{O}_S + g_P\mathcal{O}_P + g_T\mathcal{O}_T]. \quad (3)$$

Here, G_F is the Fermi constant and V_{cb} is the Cabibbo-Kobayashi-Maskawa matrix element. The effective operators are

$$\mathcal{O}_V^{LL} = (\bar{\tau}\gamma_\mu P_L \nu_\tau)(\bar{c}\gamma^\mu P_L b), \quad \mathcal{O}_S = \frac{1}{2}(\bar{\tau}P_L\nu_\tau)(\bar{c}b), \quad (4)$$

$$\mathcal{O}_V^{LR} = (\bar{\tau}\gamma_\mu P_L \nu_\tau)(\bar{c}\gamma^\mu P_R b), \quad \mathcal{O}_P = \frac{1}{2}(\bar{\tau}P_L\nu_\tau)(\bar{c}\gamma_5 b), \quad \mathcal{O}_T = (\bar{\tau}\sigma_{\mu\nu}P_L\nu_\tau)(\bar{c}\sigma^{\mu\nu}b). \quad (5)$$

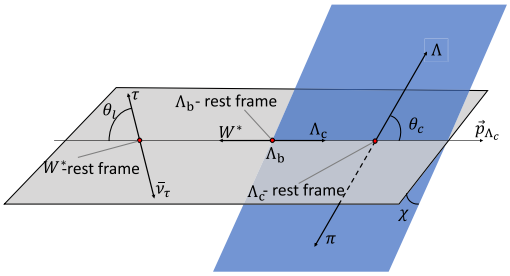

FIG. 1. Kinematics of $\Lambda_b \to \Lambda_c(\to \Lambda\pi)W^*(\to \tau\bar{\nu}_\tau)$ decay. The angles are defined following [58].

The corresponding NP Wilson coefficients are g_L, g_R, g_S, g_P, and g_T. In our analysis, we ignore the tensor operator for simplicity and only consider the vector and the scalar new physics operators. Among the operators in Eqs. (4) and (5), only O_V^{LR} cannot be mapped to a dimension-six SMEFT operator. Our goal is to find observables that can distinguish the effect of this operator from SM and from other NP operators. A large nonzero value of $\mathcal{O}(0.1\text{–}1)$ for the coefficient g_R would imply new physics beyond SMEFT.

The kinematics of the decay is shown in Fig. 1. The spin components of the particles involved in the decay $\Lambda_b \to \Lambda_c(\to \Lambda\pi)W^*(\to \tau\bar{\nu}_\tau)$ may be represented as

$$\Lambda_b(s_1, m_1) \longrightarrow \Lambda_c(s_2, \lambda_2) + W^*(s_3, \lambda_3)$$
$$\Lambda(\lambda_4) + \pi(\lambda_5) \leftarrow$$
$$\tau(\lambda_6) + \bar{\nu}_\tau(\lambda_7)\,. \leftarrow$$

Here, s_1 denotes the spin of Λ_b, and m_1 denotes its component along an arbitrarily chosen quantization axis. The spins and helicities of Λ_c and W^* in the Λ_b rest frame are denoted by (s_2, λ_2) and (s_3, λ_3), respectively. The helicities of (Λ, π) in the Λ_c rest frame are (λ_4, λ_5), while the helicities of (τ, ν_τ), in their center of mass frame, i.e., W^* rest frame, are (λ_6, λ_7). Clearly, $\lambda_5 = 0$ and $\lambda_7 = +1/2$.

A. Definitions of the angles

The angles in our analysis are defined as follows. In the rest frame of Λ_b, the Λ_c hadron makes an angle θ_1 with the spin quantization axis $\mathbf{z_1}$ of Λ_b. In this frame, the direction of Λ_c momentum is taken to be the $\mathbf{z_2}$ axis, and the opposite direction, i.e., the direction of W^* momentum, is denoted as the $\mathbf{z_3}$ axis. The x axes $(\mathbf{x_1}, \mathbf{x_2}, \mathbf{x_3})$ are chosen arbitrarily in the planes orthogonal to $(\mathbf{z_1}, \mathbf{z_2}, \mathbf{z_3})$, keeping $\mathbf{x_2} = -\mathbf{x_3}$. This fixes the directions of the y axes $(\mathbf{y_1}, \mathbf{y_2}, \mathbf{y_3})$ automatically. In the rest frame of Λ_c, the momentum of Λ is denoted by the spherical polar coordinates (θ_2, ϕ_2), while in the rest frame of W^*, the direction of τ is denoted by (θ_3, ϕ_3).

The angular distribution of the decay $\Lambda_b \to \Lambda_c(\Lambda\pi)W^*(\to \tau\overline{\nu_\tau})$ may be written in terms of helicity amplitudes [58–60] as

$$\tilde{I}(\Omega_1,\Omega_2,\Omega_3) = \sum_{m_1,m_1',\lambda_i,\lambda_j',s_3,s_3'} \Big\{ \rho_{m_1 m_1'} D^{s_1}_{m_1,\lambda_2-\lambda_3}(\Omega_1) D^{s_1*}_{m_1',\lambda_2'-\lambda_3'}(\Omega_1) H^*_{\lambda_2\lambda_3} H_{\lambda_2'\lambda_3'} D^{s_2}_{\lambda_2,\lambda_4-\lambda_5}(\Omega_2) D^{s_2*}_{\lambda_2',\lambda_4-\lambda_5}(\Omega_2) \times B^*_{\lambda_4\lambda_5} B_{\lambda_4\lambda_5} (-1)^{s_3+s_3'} D^{s_3}_{\lambda_3,\lambda_6-\lambda_7}(\Omega_3) D^{s_3'*}_{\lambda_3',\lambda_6-\lambda_7}(\Omega_3) L^*_{\lambda_6\lambda_7} L_{\lambda_6\lambda_7} \Big\}. \tag{6}$$

Here $\rho_{m_1 m_1'}$ is the density matrix for Λ_b spin quantized along $\mathbf{z_1}$. We have

$$D^j_{m,m'}(\Omega_i) \equiv e^{-im\phi_i} d^j_{m,m'}(\theta_i) e^{im'\phi_i}, \tag{7}$$

where $D^j_{m,m'}(\Omega_i)$ is Wigner's D matrix, and we have taken the Euler angles corresponding to Ω_i to be $(\phi_i, \theta_i, -\phi_i)$, using the Jacob-Wick convention [34]. Note that s_3 can take the values 0 and 1. Further, $H_{\lambda_i\lambda_j}$ and $B_{\lambda_4\lambda_5}$ are the hadronic matrix elements in the helicity basis for $\Lambda_b \to \Lambda_c(\lambda_i) W^*(\lambda_j)$ and $\Lambda_c \to \Lambda(\lambda_4)\pi(\lambda_5)$ decays, respectively, and $L_{\lambda_6\lambda_7}$ is the leptonic matrix element for $W^* \to \tau(\lambda_6)\nu_\tau(\lambda_7)$.

We assume that the initial Λ_b is unpolarized and sum over all possible spin components of Λ_b as well as integrate over the angles θ_1 and ϕ_1. This reduces the angular distribution to the form

$$I(\Omega_2,\Omega_3) = \sum_{\lambda_i,\lambda_j',s_3,s_3'} \Big\{ 2\pi\delta_{(\lambda_2-\lambda_3),(\lambda_2'-\lambda_3')} (-1)^{s_3+s_3'} H^*_{\lambda_2\lambda_3} H_{\lambda_2'\lambda_3'} D^{s_2}_{\lambda_2,\lambda_4-\lambda_5}(\Omega_2) D^{s_2*}_{\lambda_2',\lambda_4-\lambda_5}(\Omega_2) \times B^*_{\lambda_4\lambda_5} B_{\lambda_4\lambda_5} D^{s_3}_{\lambda_3,\lambda_6-\lambda_7}(\Omega_3) D^{s_3'*}_{\lambda_3',\lambda_6-\lambda_7}(\Omega_3) L^*_{\lambda_6\lambda_7} L_{\lambda_6\lambda_7} \Big\}. \tag{8}$$

Note that, since the direction of axes $\mathbf{z_2}$ and $\mathbf{z_3}$ are opposite and the direction $\mathbf{x_2} = -\mathbf{x_3}$ is arbitrary, the individual values of ϕ_2 and ϕ_3 are arbitrary, but the combination $\chi \equiv \phi_2 + \phi_3$ is physical. This is, indeed, the physical angle between the decay planes of $\Lambda_c \to \Lambda + \pi$ and $W^* \to \tau + \nu_\tau$. As a result, we get the angular distribution of the decay in terms of three physical angles: θ_2, θ_3, and χ. From now on, we refer to θ_2 as θ_c and θ_3 as θ_l. We assume that the decay $\Lambda_b \to \Lambda_c(\to \Lambda\pi)\tau\bar{\nu}_\tau$ is completely identified, so that the values of θ_c, θ_l, and χ are available for every event. Note that the three-momentum of τ can be reconstructed in the three-prong topology using the direction of τ track [46,61].

B. Hadronic and leptonic matrix elements

The hadronic matrix elements for the $\Lambda_b \to \Lambda_c W^*$ transition, in the rest frame of Λ_b, are given by [57]

$$\begin{aligned} H^V_{\lambda_2,\lambda_3} &= (1+g_L+g_R)\epsilon^{*\mu}(\lambda_3)\langle\Lambda_c(\lambda_2)|\bar{c}\gamma_\mu b|\Lambda_b\rangle, \\ H^A_{\lambda_2,\lambda_3} &= (1+g_L-g_R)\epsilon^{*\mu}(\lambda_3)\langle\Lambda_c(\lambda_2)|\bar{c}\gamma_\mu\gamma_5 b|\Lambda_b\rangle, \\ H^S_{\lambda_2,\lambda_3} &= g_S\langle\Lambda_c(\lambda_2)|\bar{c}b|\Lambda_b\rangle, \\ H^P_{\lambda_2,\lambda_3} &= g_P\langle\Lambda_c(\lambda_2)|\bar{c}\gamma_5 b|\Lambda_b\rangle. \end{aligned} \tag{9}$$

Here ϵ^μ represents the polarization vector of W^*. Only certain combinations of these hadronic matrix elements have nonzero contributions to the decay amplitude. For the vector and axial-vector currents, nonzero contributions are seen to arise only from the specific combination $H^{VA}_{\lambda_2,\lambda_3} = H^V_{\lambda_2,\lambda_3} - H^A_{\lambda_2,\lambda_3}$. Similarly, for the scalar and pseudoscalar currents, nonzero contributions come only from $H^{SP}_{\lambda_2,\lambda_3} = H^S_{\lambda_2,\lambda_3} + H^P_{\lambda_2,\lambda_3}$. The explicit expressions of the hadronic amplitudes for different values of helicities [57] are provided in Appendix A.

The amplitudes for the $\Lambda_c \to \Lambda\pi$ transition in the Λ_c rest frame are defined as

$$B_{\lambda_4\lambda_5} = \langle\Lambda(\lambda_4)\pi(\lambda_5)|\Lambda_c(\lambda_2)\rangle. \tag{10}$$

There are two independent amplitudes $B_{\frac{1}{2},0}$ and $B_{-\frac{1}{2},0}$. We do not use the analytic expressions for these amplitudes but calculate them in terms of the average decay rate $\Gamma_{\Lambda\pi}$ and the polarization asymmetry α_P, defined as [42]

$$\Gamma_{\Lambda\pi} = \frac{\sqrt{Q}}{32\pi m^3_{\Lambda_c}} \Big(|B_{\frac{1}{2},0}|^2 + |B_{-\frac{1}{2},0}|^2 \Big), \tag{11}$$

$$\alpha_P = \frac{|B_{\frac{1}{2},0}|^2 - |B_{-\frac{1}{2},0}|^2}{|B_{\frac{1}{2},0}|^2 + |B_{-\frac{1}{2},0}|^2}, \tag{12}$$

where $Q = (m^2_{\Lambda_c} - (m_\Lambda + m_\pi)^2)(m^2_{\Lambda_c} - (m_\Lambda - m_\pi)^2)$. The values of $\Gamma_{\Lambda\pi}$ and α_P are taken from measurements [62].

The leptonic amplitudes for $W^* \to \tau\bar{\nu}_\tau$ are given as

$$L^{VA}_{\lambda_6,\lambda_7} = \epsilon^\mu(\lambda_3)\langle\tau\bar{\nu}_\tau|\bar{\tau}\gamma_\mu P_L \nu_\tau|0\rangle, \tag{13}$$

$$L^{SP}_{\lambda_6,\lambda_7} = \langle \tau\bar{\nu}_\tau|\bar{\tau}P_L\nu_\tau|0\rangle. \tag{14}$$

In the rest frame of W^*, these leptonic amplitudes are [63]

$$L^{VA}_{-\frac{1}{2},\frac{1}{2}} = \sqrt{8(q^2-m_\tau^2)}, \tag{15}$$

$$L^{VA}_{\frac{1}{2},\frac{1}{2}} = \frac{m_\tau}{\sqrt{2q^2}}\sqrt{8(q^2-m_\tau^2)}, \tag{16}$$

$$L^{SP}_{-\frac{1}{2},\frac{1}{2}} = \sqrt{4(q^2-m_\tau^2)}. \tag{17}$$

Here q^2 is the invariant mass of the $(\tau,\bar{\nu}_\tau)$ pair.

C. The angular distribution

After summing over the helicities of all particles and integrating over the nonmeasurable angles, we obtain the normalized angular distribution in the form

$$\begin{aligned}\frac{1}{(d\Gamma/dq^2)}\frac{d\Gamma}{dq^2 d\cos\theta_c d\cos\theta_l d\chi} &= A_0 + A_1\cos\theta_c + A_2\cos\theta_l + A_3\cos\theta_c\cos\theta_l \\ &+ A_4\cos^2\theta_l + A_5\cos\theta_c\cos^2\theta_l + A_6\sin\theta_c\sin\theta_l\cos\chi \\ &+ A_7\sin\theta_c\sin\theta_l\sin\chi + A_8\sin\theta_c\sin\theta_l\cos\theta_l\cos\chi \\ &+ A_9\sin\theta_c\sin\theta_l\cos\theta_l\sin\chi.\end{aligned} \tag{18}$$

The coefficients A_0–A_9 in Eq. (18) can be extracted from a fit to the observed angular distribution or by the method of angular moments [64]. We have provided the weighting functions required to extract these coefficients in Appendix B. The coefficients A_0–A_9, which we refer to as the angular observables, are given in Eqs. (20)–(29), in terms of the total decay width

$$\begin{aligned}\Gamma_0 \equiv \frac{2}{3}\Big\{&(m_\tau^2+2q^2)\Big(|H^{VA}_{-\frac{1}{2},-1}|^2 + |H^{VA}_{-\frac{1}{2},0}|^2 + |H^{VA}_{\frac{1}{2},0}|^2 + |H^{VA}_{\frac{1}{2},1}|^2\Big) \\ &+ 3\Big(|m_\tau H^{VA}_{-\frac{1}{2},t} + \sqrt{q^2}H^{SP}_{-\frac{1}{2},t}|^2 + |m_\tau H^{VA}_{\frac{1}{2},t} + \sqrt{q^2}H^{SP}_{\frac{1}{2},t}|^2\Big)\Big\}.\end{aligned} \tag{19}$$

$$\begin{aligned}A_0 = \frac{1}{\Gamma_0}\Big(&\frac{1}{2}(m_\tau^2+q^2)|H^{VA}_{\frac{1}{2},1}|^2 + \frac{1}{2}(m_\tau^2+q^2)|H^{VA}_{-\frac{1}{2},-1}|^2 + |m_\tau H^{VA}_{\frac{1}{2},t} + \sqrt{q^2}H^{SP}_{\frac{1}{2},t}|^2 \\ &+ |m_\tau H^{VA}_{-\frac{1}{2},t} + \sqrt{q^2}H^{SP}_{-\frac{1}{2},t}|^2 + q^2|H^{VA}_{\frac{1}{2},0}|^2 + q^2|H^{VA}_{-\frac{1}{2},0}|^2\Big),\end{aligned} \tag{20}$$

$$\begin{aligned}A_1 = \frac{\alpha_P}{2\Gamma_0}\Big(&(m_\tau^2+q^2)|H^{VA}_{\frac{1}{2},1}|^2 + (m_\tau^2+q^2)|H^{VA}_{-\frac{1}{2},-1}|^2 - 2|m_\tau H^{VA}_{\frac{1}{2},t} + \sqrt{q^2}H^{SP}_{\frac{1}{2},t}|^2 \\ &+ 2|m_\tau H^{VA}_{-\frac{1}{2},t} + \sqrt{q^2}H^{SP}_{-\frac{1}{2},t}|^2 - 2q^2|H^{VA}_{\frac{1}{2},0}|^2 + 2q^2|H^{VA}_{-\frac{1}{2},0}|^2\Big),\end{aligned} \tag{21}$$

$$A_2 = -\frac{1}{\Gamma_0}\Big(q^2|H^{VA}_{\frac{1}{2},1}|^2 + q^2|H^{VA}_{-\frac{1}{2},-1}|^2 - 2\mathrm{Re}\Big\{\Big(m_\tau H^{VA}_{\frac{1}{2},0}\Big(m_\tau H^{VA}_{\frac{1}{2},t} + \sqrt{q^2}H^{SP}_{\frac{1}{2},t}\Big)^* + m_\tau H^{VA}_{-\frac{1}{2},0}\Big(m_\tau H^{VA}_{-\frac{1}{2},t} + \sqrt{q^2}H^{SP}_{-\frac{1}{2},t}\Big)^*\Big)\Big\}\Big), \tag{22}$$

$$A_3 = -\frac{\alpha_P}{\Gamma_0}(q^2|H^{VA}_{\frac{1}{2},1}|^2 + q^2|H^{VA}_{-\frac{1}{2},-1}|^2 + 2m_\tau\mathrm{Re}\Big\{\Big(H^{VA}_{\frac{1}{2},0}\Big(m_\tau H^{VA}_{\frac{1}{2},t} + \sqrt{q^2}H^{SP}_{\frac{1}{2},t}\Big)^* - H^{VA}_{-\frac{1}{2},0}\Big(m_\tau H^{VA}_{-\frac{1}{2},t} + \sqrt{q^2}H^{SP}_{-\frac{1}{2},t}\Big)^*\Big)\Big\}\Big), \tag{23}$$

$$A_4 = -\frac{1}{2\Gamma_0}(m_\tau^2-q^2)\Big(|H^{VA}_{\frac{1}{2},1}|^2 + |H^{VA}_{-\frac{1}{2},-1}|^2 - 2\Big(|H^{VA}_{\frac{1}{2},0}|^2 + |H^{VA}_{-\frac{1}{2},0}|^2\Big)\Big), \tag{24}$$

$$A_5 = \frac{\alpha_P}{\Gamma_0}(m_\tau^2-q^2)\Big(2|H^{VA}_{\frac{1}{2},0}|^2 - |H^{VA}_{\frac{1}{2},1}|^2 + |H^{VA}_{-\frac{1}{2},-1}|^2 - 2|H^{VA}_{-\frac{1}{2},0}|^2\Big), \tag{25}$$

$$\begin{aligned}A_6 = -\frac{\alpha_P}{\sqrt{2}\Gamma_0}2\mathrm{Re}\Big\{&\Big(H^{VA}_{-\frac{1}{2},-1}\Big)^*\Big(m_\tau\Big(m_\tau H^{VA}_{\frac{1}{2},t} + \sqrt{q^2}H^{SP}_{\frac{1}{2},t}\Big) + q^2 H^{VA}_{\frac{1}{2},0}\Big) \\ &+ \Big(H^{VA}_{\frac{1}{2},1}\Big)^*\Big(q^2 H^{VA}_{-\frac{1}{2},0} - m_\tau\Big(m_\tau H^{VA}_{-\frac{1}{2},t} + \sqrt{q^2}H^{SP}_{-\frac{1}{2},t}\Big)\Big)\Big\},\end{aligned} \tag{26}$$

$$A_7 = -\frac{\alpha_P}{\sqrt{2}\Gamma_0} 2\mathrm{Im}\left\{ \left(H^{VA}_{\frac{1}{2},1}\right)^* \left(q^2 H^{VA}_{-\frac{1}{2},0} - m_\tau \left(m_\tau H^{VA}_{-\frac{1}{2},t} + \sqrt{q^2} H^{SP}_{-\frac{1}{2},t} \right) \right) - \left(H^{VA}_{-\frac{1}{2},-1}\right)^* \left(m_\tau \left(m_\tau H^{VA}_{\frac{1}{2},t} + \sqrt{q^2} H^{SP}_{\frac{1}{2},t} \right) + q^2 H^{VA}_{\frac{1}{2},0} \right) \right\}, \tag{27}$$

$$A_8 = \frac{\alpha_P}{\sqrt{2}\Gamma_0} (m_\tau^2 - q^2) 2\mathrm{Re}\left\{ \left(H^{VA}_{-\frac{1}{2},-1} \left(H^{VA}_{\frac{1}{2},0}\right)^* - H^{VA}_{-\frac{1}{2},0} \left(H^{VA}_{\frac{1}{2},1}\right)^* \right) \right\}, \tag{28}$$

$$A_9 = \frac{\alpha_P}{\sqrt{2}\Gamma_0} (m_\tau^2 - q^2) 2\mathrm{Im}\left(H^{VA}_{-\frac{1}{2},-1} \left(H^{VA}_{\frac{1}{2},0}\right)^* + H^{VA}_{\frac{1}{2},1} \left(H^{VA}_{-\frac{1}{2},0}\right)^* \right). \tag{29}$$

Note that, while A_7 and A_9 change sign under $g_R \leftrightarrow g_R^*$ (see the explicit expressions for $H^{VA}_{\lambda_2,\lambda_3}$ in Appendix A), all the other angular observables are invariant under this interchange.

The mapping of the angular observables above to the ones calculated in earlier literature [40] has been provided in Appendix C. In the next section, we will discuss the utility of these angular observables for identifying physics beyond SM and physics beyond SMEFT.

III. OBSERVABLES AND NUMERICAL RESULTS

Each of the coefficients A_0–A_9 in Eq. (18) can be measured if the information about the angles θ_c, θ_l, χ and the leptonic invariant mass square q^2 are known. In this section, we consider four NP scenarios g_L, g_R, s_L, and s_R, where only the corresponding complex NP parameter g_L, g_R, s_L, and s_R, respectively, is nonzero. Here we have defined

$$s_L = (g_S - g_P)/2 \quad \text{and} \quad s_R = (g_S + g_P)/2. \tag{30}$$

First, we identify the parameter values in all scenarios that give a reasonable fit to the above five observables, i.e., a χ^2 less than a predecided value or a p value greater than a predecided minimum. Later, we check if the predictions of the angular observables in the g_R scenario can be mimicked by any of the allowed set of parameters in the other scenarios.

A. Constraining NP parameters based on meson decay observations

In order to obtain the allowed parameter values in each scenario, we perform a χ^2 fit for the corresponding NP parameter. The χ^2 is defined as

$$\chi^2 \equiv \sum_{i,j} (O_i^{\mathrm{th}} - O_i^{\mathrm{exp}}) \mathrm{Cov}_{ij}^{-1} (O_j^{\mathrm{th}} - O_j^{\mathrm{exp}}). \tag{31}$$

The experimentally measured central values of O_i^{exp} and their uncertainties $\Delta O_i^{\mathrm{exp}}$ are shown in Table I. The theoretical values of these observables are calculated based on [65]. The covariance matrix Cov_{ij} is defined as

$$\mathrm{Cov}_{ij} \equiv \Delta O_i^{\mathrm{exp}} \rho_{ij} \Delta O_j^{\mathrm{exp}} + \Delta O_i^{\mathrm{th}} \delta_{ij} \Delta O_j^{\mathrm{th}}, \tag{32}$$

where ρ_{ij} is the correlation between ith and jth observables. For a pair of independent measurements i and j, we have $\rho_{ij} = \delta_{ij}$. For the measurements of $i \equiv R_D$ and $j \equiv R_{D^*}$, we have taken $\rho_{ij} = -0.37$ [66]. We further ignore the theoretical uncertainties as they are much smaller compared to the experimental uncertainties [65].

For any fixed value of the complex parameters g_L, g_R, s_L, and s_R, we calculate the χ^2 using five observables as listed in Table I. The goodness of fit for each of the parameter values may be expressed in terms of χ^2, p values, confidence levels, or number of σ's. Since we are determining the goodness of fit for each NP parameter value independently, the number of degrees of freedom (d.o.f.) is the same as the number of observables, i.e., five. For 5 d.o.f., the correspondence among these four measures

TABLE I. Current experimental values and SM predictions of the observables R_D, R_D^*, $R_{j/\psi}$, $P_\tau^{D^*}$, and $F_L^{D^*}$.

Observable	Experimental value	SM value
R_D	0.357 ± 0.029 [14–16,66–68]	0.298 ± 0.004 [66,68–72]
R_D^*	0.284 ± 0.012 [14–17,61,66,68,73–76]	0.254 ± 0.005 [66,68,77–79]
$R_{j/\psi}$	$0.71 \pm 0.17 \pm 0.18$ [18]	0.258 ± 0.004 [80,81]
$P_\tau^{D^*}$	$-0.38 \pm 0.51 \pm 0.21$ [75,76]	-0.497 ± 0.013 [82]
$F_L^{D^*}$	$0.60 \pm 0.08 \pm 0.035$ [83]	0.46 ± 0.04 [84]

TABLE II. Correspondence among the four measures of the goodness of fit, with 5 degrees of freedom.

Sigma	CL (%)	p value	χ^2
1σ	68.3	0.317	5.89
1.64σ	90	0.10	9.24
2σ	95.45	0.0455	11.31

of goodness of fit is given in Table II. Thus, stating that an NP parameter value is allowed at 2σ or 95.45% CL is equivalent to stating that its p value $p > 0.0455$ or $\chi^2 < 11.31$.

In Fig. 2, we show the NP parameter values allowed at 1σ, 1.64σ, and 2σ in the four scenarios under consideration. The best-fit points in each scenario, calculated using the Python package IMINUIT [85], have been indicated in this figure as well as in Table III. It is observed that, in the scenarios g_L, g_R, and s_L, there are parameter values allowed at 1σ. However, no parameter values in the s_R scenario are allowed even at 1.64σ, though there are some values allowed at 2σ. The SM itself has a p value of 0.00045 and is disfavored at more than 3.5σ.

So far, we have not considered the observable $\mathcal{B}(B_c \to \tau\bar{\nu}_\tau)$, which is very sensitive to the scalar NP operators [39]. The SM value for $\mathcal{B}(B_c \to \tau\bar{\nu}_\tau)$ is $\simeq 2.2\%$ [62]. Experimentally, the $B_c \to \tau\bar{\nu}_\tau$ branching fraction is not yet measured. In [86], an upper bound $\mathcal{B}(B_c \to \tau\bar{\nu}_\tau) < 30\%$ is evaluated from the missing decay width of the B_c meson. On the other hand, an upper bound $\mathcal{B}(B_c \to \tau\bar{\nu}_\tau) < 10\%$ is obtained in [87] using data from the large electron positron (LEP) experiment. However, it has been pointed out [38,39,88] that the p_T dependence of the fragmentation function $b \to B_c$ has been overlooked in [87] and thus the bound may be overestimated. In [38], the authors suggest a more conservative bound $\mathcal{B}(B_c \to \tau\bar{\nu}_\tau) < 60\%$. We show the contours corresponding to the upper bounds $\mathcal{B}(B_c \to \tau\bar{\nu}_\tau) < 60\%, 30\%$, and 10% in Fig. 2 to indicate the values of s_L and s_R, which would remain valid even with these constraints. These fit results match reasonably with earlier literature [65,89] and with the recent fit [90],

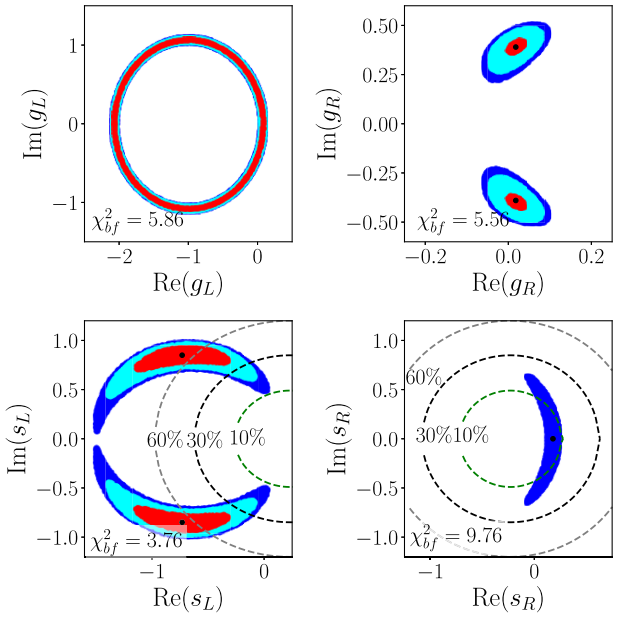

FIG. 2. Regions allowed in the parameter space of g_L, g_R, s_L, and s_R in the absence of any restriction on $\mathcal{B}(B_c \to \tau\bar{\nu}_\tau)$. The red, cyan, and blue regions are allowed at 1σ, 1.64σ, and 2σ, respectively (5 d.o.f.). The black dots represent the best-fit values of the NP parameters. Note that the χ^2 values in the g_L scenario are degenerate along the red circular region, and there is no single best-fit value. The dashed (gray, black, green) contours indicate the allowed values of s_L and s_R corresponding to the upper bound $\mathcal{B}(B_c \to \tau\bar{\nu}_\tau) < (60\%, 30\%, 10\%)$. For g_L and g_R, even the contours for $\mathcal{B}(B_c \to \tau\bar{\nu}_\tau) < 10\%$ are outside the range shown in the figure.

where g_L, s_L, and s_R scenarios were analyzed. In the future, the FCC-ee and CEPC experiments expect to directly measure $\mathcal{B}(B_c \to \tau\bar{\nu}_\tau)$ at the $\mathcal{O}(1\%)$ level [91,92]. In our analysis, we first present our results with the condition $\mathcal{B}(B_c \to \tau\bar{\nu}_\tau) < 30\%$, and later we see the impact of a stronger bound $\mathcal{B}(B_c \to \tau\bar{\nu}_\tau) < 10\%$.

It is not possible in SMEFT to have as large a value of g_R as mentioned in Table III. If such a large value of g_R is measured experimentally, it would imply physics beyond SMEFT and hence a nonlinear realization of the EW

TABLE III. Best-fit values of the NP parameters for the scenarios g_L, g_R, s_L, and s_R, along with the corresponding χ^2 and p values (5 d.o.f.) for these best-fit points, for unrestricted $\mathcal{B}(B_c \to \tau\bar{\nu}_\tau)$ (left), for $\mathcal{B}(B_c \to \tau\bar{\nu}_\tau) < 30\%$ (center), and for $\mathcal{B}(B_c \to \tau\bar{\nu}_\tau) < 10\%$ (right). Note that restricting $\mathcal{B}(B_c \to \tau\bar{\nu}_\tau)$ does not affect the best-fit points of g_L, g_R, and s_R. The asterisk for the best-fit value in the g_L scenario indicates that there is no single best-fit point (see Fig. 2).

	$\mathcal{B}(B_c \to \tau\bar{\nu}_\tau)$ unrestricted			$\mathcal{B}(B_c \to \tau\bar{\nu}_\tau) < 30\%$			$\mathcal{B}(B_c \to \tau\bar{\nu}_\tau) < 10\%$		
Scenario	Best-fit	χ^2_{bf}	p value$_{(bf)}$	Best-fit	χ^2_{bf}	p value$_{(bf)}$	Best-fit	χ^2_{bf}	p value$_{(bf)}$
SM	⋯	22.35	0.00045	⋯	22.35	0.00045	⋯	22.35	0.00045
g_L	$*$	5.86	0.32	$*$	5.86	0.32	$*$	5.86	0.32
g_R	$0.018 \pm 0.39i$	5.56	0.35	$0.018 \pm 0.39i$	5.56	0.35	$0.018 \pm 0.39i$	5.56	0.35
s_L	$-0.73 \pm 0.85i$	3.76	0.58	$-0.22 - 0.72i$	7.24	0.20	$0.04 - 0.45i$	11.78	0.04
s_R	$0.18 + 0.00i$	9.76	0.08	$0.18 + 0.00i$	9.76	0.08	$0.18 + 0.00i$	9.76	0.08

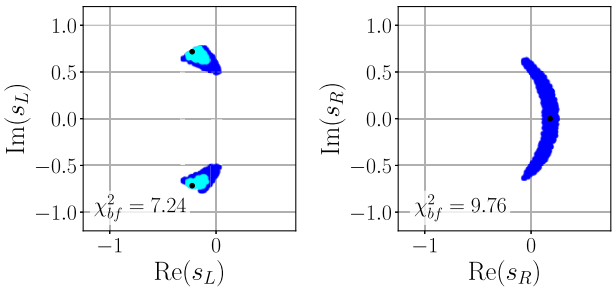

FIG. 3. Allowed regions in the parameter spaces of s_L and s_R, with the upper bound $\mathcal{B}(B_c \to \tau\bar{\nu}_\tau) < 30\%$. The cyan and blue regions are allowed at 1.64σ and 2σ, respectively (5 d.o.f.).

symmetry. In the following, we see how such a value of g_R can be identified from the angular observables and how its effect can be distinguished from the other NP parameters.

B. Angular observables in $\Lambda_b \to \Lambda_c(\to \Lambda\pi)\tau\bar{\nu}_\tau$ for BSM and beyond-SMEFT signatures

Our aim is to look for confirmed signals of any kind of NP and to further identify whether this NP needs terms beyond SMEFT for its description. We proceed in two steps.

In the first step, we check for each of the observables whether the effects of g_R at its best-fit value can be distinguished from the SM predictions. The 2σ uncertainties on the observables due to the hadronic form factors are incorporated using the z-expansion coefficients and their correlated uncertainties as given in [49]. We also include the effect of the uncertainty in the measurement of the polarization asymmetry α_P [62].

In the second step, in order to distinguish the effects of g_R from the effects of g_L, s_L, and s_R, we vary these NP parameters within their 2σ-allowed ranges, while continuing to include the uncertainties due to the hadronic form factors and α_P. When the band of g_R is nonoverlapping with the bands of other scenarios in some q^2 range, there is potential for identification of the g_R scenario.

In this subsection, we take the upper bound on $\mathcal{B}(B_c \to \tau\bar{\nu}_\tau)$ to be a sharp cut off at 30%, i.e., we calculate the χ^2 values for only those points in the parameter space for which $\mathcal{B}(B_c \to \tau\bar{\nu}_\tau) < 30\%$. It is observed that there is no change in the allowed regions for g_L, g_R, and s_R compared to Fig. 2. However, for s_L, the allowed region gets severely restricted and no value of s_L is allowed at 1σ. The allowed regions in the s_L and s_R parameter spaces are shown in Fig. 3. Note that with this upper bound, the g_R scenario gives a better χ^2 fit than the other scenarios. In particular, $\chi^2_{bf}(g_R) < \chi^2_{bf}(s_L)$, which was not the case for unrestricted $\mathcal{B}(B_c \to \tau\bar{\nu}_\tau)$.

We now proceed to calculate the decay width and the angular observables in $\Lambda_b \to \Lambda_c(\to \Lambda\pi)\tau\bar{\nu}_\tau$ as functions of q^2, and compare the predictions of the NP scenarios g_L, g_R, s_L, and s_R.

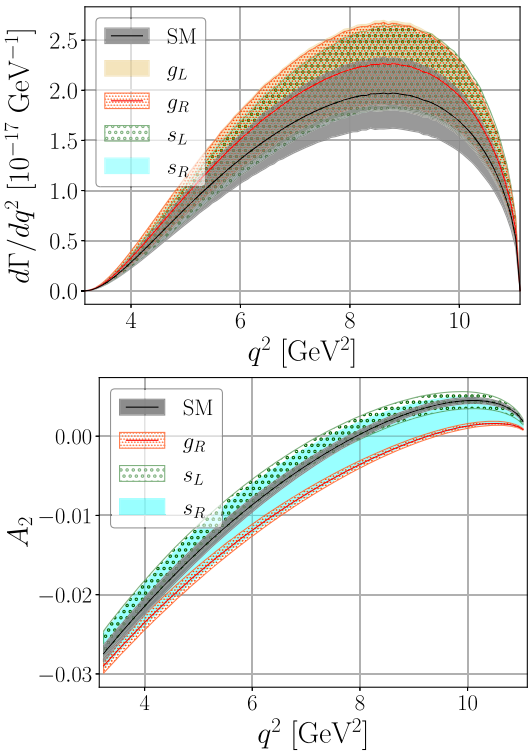

FIG. 4. Top: the differential decay rate $d\Gamma/dq^2$ as a function of q^2, with SM and the NP scenarios g_L, g_R, s_L, and s_R. Bottom: the angular observable A_2 (the forward-backward asymmetry) as a function of q^2, with SM and the NP scenarios g_R, s_L, and s_R. For both the observables, the values of g_L, s_L, and s_R are varied within their 2σ-allowed ranges, while g_R is kept fixed at its best-fit value. For each scenario, 2σ uncertainties due to the hadronic form factors and the polarization asymmetry α_P have been included. The calculation of $d\Gamma/dq^2$ also includes the uncertainty in V_{cb}. The bound $\mathcal{B}(B_c \to \tau\bar{\nu}_\tau) < 30\%$ is imposed for both these plots.

1. Decay width $d\Gamma/dq^2$

In the top panel of Fig. 4, we show the effects of g_L, g_R, s_L, and s_R on $d\Gamma/dq^2$. The best-fit value of g_R and the 2σ-allowed values of g_L, s_L, and s_R are taken. The 2σ uncertainties due to the hadronic form factors α_P and V_{cb} are included. We use the exclusive measurement of V_{cb} [62]. Note that it will be almost impossible to distinguish g_R from the SM or other NP scenarios, using only $d\Gamma/dq^2$.

2. Angular observables

We divide the ten angular observables A_0, ... ,A_9 in five subsets: (i) A_0 and A_4, (ii) A_2, (iii) A_1, A_3, and A_5, (iv) A_6 and A_8, (v) A_7 and A_9. We then explore the effects of the NP parameters g_L, g_R, s_L, and s_R on these observables, as functions of q^2. Note that when the NP appears only through g_L, Eq. (A4) indicates that all the hadronic matrix elements $H^{VA}_{\lambda,\lambda'}$ get multiplied by a common factor $(1 + g_L)$. As a result, in the angular observables given in

Eqs. (20)–(29), the dependence on g_L cancels out completely. Consequently, the angular observables will not be affected by g_L. Therefore, in the following sections we only focus on the effects of g_R, s_L, and s_R. Note that the uncertainty in V_{cb} gets canceled out in all the angular observables.

(i) A_0 and A_4: These two angular observables are the coefficients of the constant term and $\cos^2\theta_l$ in Eq. (18), respectively. They are trivially related as $A_0 + A_4/3 = 1/2$. Even though they are easier to measure experimentally, we find that they cannot distinguish the effects of nonzero g_R from SM when we include the uncertainties due to hadronic form factors.

(ii) A_2: This is the coefficient of the term $\cos\theta_l$ in Eq. (18). This observable corresponds to the forward-backward asymmetry $A_{\rm FB}$ with respect to θ_l. The bottom panel of Fig. 4 shows the effects of g_R, s_L, and s_R on A_2. As can be observed from the figure, the effects of g_R can be distinguished from the SM and s_L scenario if g_R takes its best-fit value. However, the g_R scenario overlaps with the s_R scenario, which means that the effect of the best-fit g_R value cannot be distinguished from that of s_R. Note that the zero crossing of A_2 shifts to higher values of q^2 compared to the SM in the g_R scenario, as has been observed earlier for $A_{\rm FB}$ [52,56].

(iii) A_1, A_3, and A_5: These are the coefficients of the angular functions that are linear in $\cos\theta_c$. These angular observables are linear in the polarization asymmetry α_P as can be seen from Eqs. (21), (23), and (25). Because of the large uncertainty in the measured value $\alpha_P = -0.84 \pm 0.09$ [62], A_1, A_3, and A_5 individually cannot distinguish the effects of g_R from those of the other scenarios. Taking the ratios $R_{3,1} \equiv A_3/A_1$ and $R_{3,5} \equiv A_3/A_5$ cancels the uncertainty due to α_P. These ratios would help in distinguishing the g_R scenario from SM at higher q^2 values. This may be seen in Fig. 5. However, these ratios would not be able to distinguish g_R from the other NP scenarios.

(iv) A_6 and A_8: The angular observables A_6 and A_8 are the coefficients of the angular terms linear in $\cos\chi$. These observables are also linear in α_P, and hence individually they are not very suitable for identifying the effects of g_R. We construct the ratio $R_{6,8} \equiv A_6/A_8$ and show its dependence on NP parameters in the top panel of Fig. 6. This ratio would only marginally help in separating the effects of g_R from SM at higher q^2 values and would not be able to distinguish from the other NP scenarios.

(v) A_7 and A_9: These observables are associated with angular functions that are linear in $\sin\chi$ and interchange sign under $g_R \leftrightarrow g_R^*$. We find that A_9 is identically zero in the SM as well as in all NP scenarios considered here. However, A_7, which vanishes in the SM, can be significantly nonzero in NP scenarios. In particular, the g_R scenario, at its best-fit point as given in Table III, can give a nonzero value of A_7 that can be distinguished from the SM as well as from the s_L and s_R scenarios, as shown in Fig. 6. Note that A_7 is the only angular observable sensitive to the sign of $\mathrm{Im}(g_R)$.

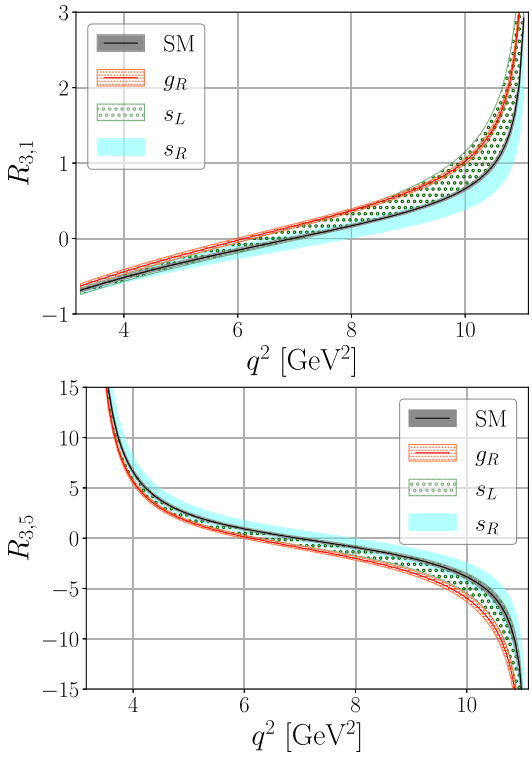

FIG. 5. The ratios $R_{3,1}$ (top panel) and $R_{3,5}$ (bottom panel) as functions of q^2, with SM and the NP scenarios g_R, s_L, and s_R. The values of s_L and s_R are varied within their 2σ-allowed ranges, while g_R is kept fixed at its best-fit value. For each scenario, 2σ uncertainties due to the hadronic form factors and the polarization asymmetry α_P have been included. The bound $\mathcal{B}(B_c \to \tau\bar{\nu}_\tau) < 30\%$ is imposed for both these plots.

We summarize the discussion in this section in Table IV, where we show the effectiveness of the angular observables and their ratios in distinguishing the effects of the best-fit g_R from the SM and from the NP scenarios g_L, s_L, and s_R. If the band of predicted values of an observable for the best-fit value of g_R does not overlap with the band corresponding to any of the other scenarios in some q^2 range, we put a tick mark in the corresponding cell. If the nonoverlapping q^2 range is very small, then we add a cross in parentheses. If the g_R prediction band always overlaps with the other scenario, we put only a cross in the corresponding cell.

For $\mathcal{B}(B_c \to \tau\bar{\nu}_\tau) < 30\%$, Table IV indicates:

(i) The observable A_2 can distinguish the effects of the best-fit value of g_R from the SM as well as from the NP scenarios g_L and s_L, but not from s_R.

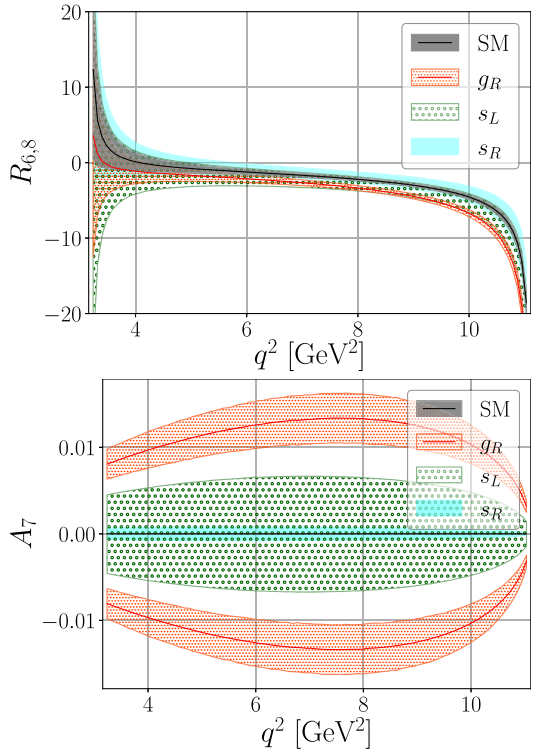

FIG. 6. The ratios $R_{6,8}$ (top) and the angular observable A_7 (bottom) as functions of q^2, with SM and the NP scenarios g_R, s_L, and s_R. The values of s_L and s_R are varied within their 2σ-allowed ranges, while g_R kept fixed at its best-fit value as given in Table III. For each scenario, 2σ uncertainties due to the hadronic form factors and the polarization asymmetry α_P have been included. The bound $\mathcal{B}(B_c \to \tau\bar{\nu}_\tau) < 30\%$ is imposed for both these plots.

(ii) The ratios $R_{3,1}$, $R_{3,5}$, and $R_{6,8}$ can distinguish the g_R scenario from SM and g_L, while failing to distinguish it from the s_L or s_R scenario.
(iii) Only the angular observable A_7 can cleanly distinguish the g_R scenario from the SM as well as from all the other NP scenarios.

C. Impact of a tighter bound on $\mathcal{B}(B_c \to \tau\bar{\nu}_\tau)$

In Sec. III B, we have analyzed the efficacy of the angular observables in distinguishing the g_R scenario from other NP scenarios, considering the NP parameter spaces restricted by $\mathcal{B}(B_c \to \tau\bar{\nu}_\tau) < 30\%$. In this section, we take a tighter bound $\mathcal{B}(B_c \to \tau\bar{\nu}_\tau) < 10\%$ and discuss the effectiveness of the angular observables in distinguishing the effect of g_R. The allowed parameter spaces for g_L and g_R remain the same as in Fig. 2. The s_L parameter space is totally excluded at 2σ, while a small s_R region around the best-fit value $s_{R,bf} = 0.18$ stays as shown in Fig. 7.

The decay width $d\Gamma/dq^2$, the angular observables A_2, A_7, and the ratios $R_{3,1}$, $R_{3,5}$, and $R_{6,8}$ are shown in Fig. 8. With the tighter boundary condition $\mathcal{B}(B_c \to \tau\bar{\nu}_\tau) < 10\%$, large regions of s_L and s_R parameter space are disallowed.

TABLE IV. The effectiveness of angular observables and their ratios in distinguishing the g_R scenario from the SM and other NP scenarios. Results for $\mathcal{B}(B_c \to \tau\bar{\nu}_\tau) < 30\%$ and $\mathcal{B}(B_c \to \tau\bar{\nu}_\tau) < 10\%$ are shown.

	Scenario					
	$\mathcal{B}(B_c \to \tau\bar{\nu}_\tau) < 30\%$			$\mathcal{B}(B_c \to \tau\bar{\nu}_\tau) < 10\%$		
Observable	SM, g_L	s_L	s_R	SM, g_L	s_L	s_R
$d\Gamma/dq^2$	✗	✗	✗	✗	✓	✗
A_0	✗	✗	✗	✗	✓	✗
A_1	✗	✗	✗	✗	✓	✗
A_2	✓	✓(×)	✗	✓	✓	✗
A_3	✓(×)	✗	✗	✓(×)	✓	✓(×)
A_4	✗	✗	✗	✗	✓	✗
A_5	✗	✗	✗	✗	✓	✗
A_6	✗	✗	✗	✗	✓	✗
A_7	✓	✓	✓	✓	✓	✓
A_8	✗	✗	✗	✗	✓	✗
A_3/A_1	✓	✗	✗	✓	✓	✓
A_3/A_5	✓	✓(×)	✗	✓	✓	✓
A_6/A_8	✓	✓(×)	✗	✓	✓	✓(×)

As a result, a clear separation between the g_R scenario and the s_L, s_R scenarios is possible for multiple angular observables.

(i) The angular observable A_7 and the ratios $R_{3,1}$ and $R_{3,5}$ can cleanly distinguish the effect of best-fit g_R from the SM as well as from all the other NP scenarios considered here.
(ii) The ratio $R_{6,8}$ can distinguish g_R from the other scenarios at higher q^2 values.

In the right half of Table IV, we summarize the results for all the angular observables and ratios with the condition $\mathcal{B}(B_c \to \tau\bar{\nu}_\tau) < 10\%$. Note that we put a tick mark for all observables in the s_L scenario because, with the condition $\mathcal{B}(B_c \to \tau\bar{\nu}_\tau) < 10\%$, there is no s_L value allowed at 2σ. In Appendix D, we show a comparison between the results obtained with the two upper bounds $\mathcal{B}(B_c \to \tau\bar{\nu}_\tau) < 30\%$

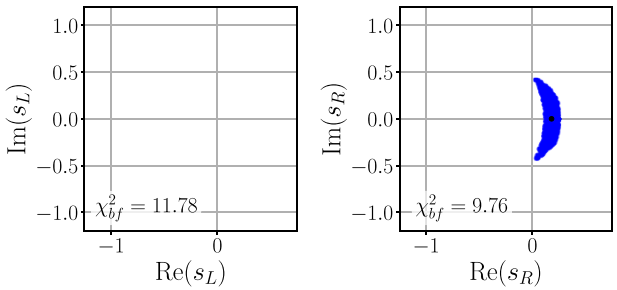

FIG. 7. Allowed regions for s_L and s_R including the upper bound $\mathcal{B}(B_c \to \tau\bar{\nu}_\tau) < 10\%$. There are no s_L values allowed at 2σ. The blue region for s_R corresponds to the parameter space allowed at 2σ (but not at 1.64σ).

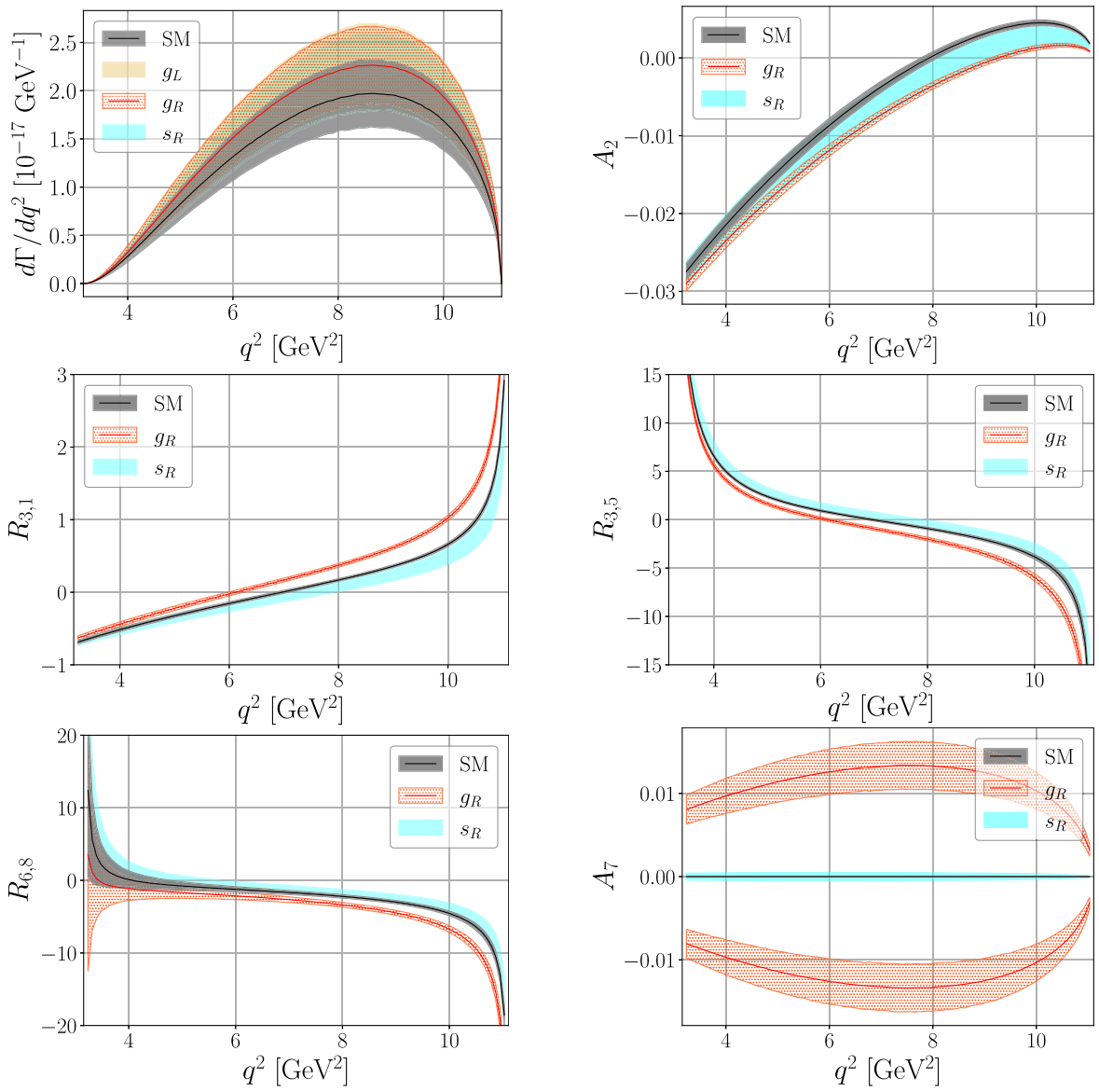

FIG. 8. The decay width $d\Gamma/dq^2$, the angular observables A_2, A_7, and the ratios $R_{3,1}$, $R_{3,5}$, and $R_{6,8}$ for $\mathcal{B}(B_c \to \tau\bar{\nu}_\tau) < 10\%$ in the SM and in the NP scenarios g_L, g_R, and s_R. The values of g_L and s_R are varied within their 2σ-allowed range, while g_R is kept fixed at its best-fit value as given in Table III. Note that there is no s_L value allowed at 2σ with this upper bound on $\mathcal{B}(B_c \to \tau\bar{\nu}_\tau)$. For all observables except $d\Gamma/dq^2$, the results for g_L are the same as those for the SM. For each scenario, 2σ uncertainties due to the hadronic form factors and the polarization asymmetry α_P have been included.

and $\mathcal{B}(B_c \to \tau\bar{\nu}_\tau) < 10\%$ for all points in the 2σ-allowed region of g_R.

Note that this analysis has been performed in the idealized limit of a perfect detector and a large number of events. The systematic and statistical uncertainties in the experiment are not taken into account. However, the results above are expected to provide a good indication of which observables and which q^2 bins would be useful in distinguishing the g_R scenario from the rest. Such a distinction will enable us to identify the presence of non-SMEFT contributions.

IV. CONCLUDING REMARKS

The present measurements of production and decay channels of the Higgs boson at the LHC are consistent with the SM Higgs mechanism of EW symmetry breaking. As a result, SMEFT is often taken to be the default EFT description above the electroweak scale. However, more general EFT descriptions such as HEFT, where the EW symmetry $SU(2)_L \times U(1)_Y$ is realized nonlinearly, are still possible. In this paper, we explore whether it is possible to identify HEFT signals that cannot be mimicked by operators allowed in SMEFT. We restrict ourselves to

scalar and vector NP operators, neglecting any tensor contributions.

We focus on the flavor physics sector, in particular, on the six-dimensional flavor nonuniversal LEFT operator $O_V^{LR} \equiv (\bar{\tau}\gamma^\mu P_L \nu_\tau)(\bar{c}\gamma_\mu P_R b)$ which is relevant for $b \to c\tau\nu_\tau$ processes. This operator can arise from a six-dimensional HEFT operator. However, it appears in SMEFT only at dimension-eight and hence its contribution would be suppressed by an extra factor of v^2/Λ^2. Therefore, a large contribution from this operator would prefer HEFT over SMEFT as the correct BSM description.

The principle of EFTs is that any operator that is not explicitly forbidden by a symmetry must be taken into account, which is the case for O_V^{LR} in a beyond-SMEFT scenario. Therefore, the consideration of this operator becomes mandatory even in the absence of a UV-complete model. There are also specific models, like the nonstandard-Higgs model with a strongly coupled scalar [32] and the one with a W' that couples to right-handed quarks and left-handed leptons [56] that give rise to the O_V^{LR} operator.

The decay $\Lambda_b \to \Lambda_c(\Lambda\pi)\tau\bar{\nu}_\tau$, when fully reconstructed, can be written in terms of an angular distribution in three angles. The coefficients of these angular terms, $A_0, \ldots, A_9$, can act as angular observables where information about NP is encoded. We calculate this angular distribution in terms of helicity amplitudes and compare the values of the above angular observables in scenarios with (i) only SM, (ii) NP with nonzero coefficient g_R of O_V^{LR}, (iii) NP with nonzero coefficient g_L of $O_V^{LL} \equiv (\bar{\tau}\gamma^\mu P_L \nu_\tau)(\bar{c}\gamma_\mu P_L b)$, and (iv) NP with new scalar and pseudoscalar operators parametrized by nonzero values of s_L and s_R. The identification of the g_R scenario would indicate the need for a HEFT description, i.e., for going beyond SMEFT.

We find that the angular observables A_2, A_7 and the ratios $R_{3,1} \equiv A_3/A_1$, $R_{3,5} \equiv A_3/A_5$, and $R_{6,8} \equiv A_6/A_8$ are, in principle, capable of distinguishing the effects of g_R from those of the SM and g_L scenarios. These can thus indicate the presence of BSM physics. It is observed that their effectiveness strongly depends on the constraints on the branching ratio $\mathcal{B}(B_c \to \tau\bar{\nu}_\tau)$. For a weaker bound $\mathcal{B}(B_c \to \tau\bar{\nu}_\tau) < 30\%$, only the angular observable A_7 can cleanly distinguish the effects of g_R from those of the s_L and s_R scenarios as well. However, if a tighter bound $\mathcal{B}(B_c \to \tau\bar{\nu}_\tau) < 10\%$ can be imposed, we find that, along with A_7, the ratios $R_{3,1}$, $R_{3,5}$, and $R_{6,8}$ could also indicate distinct effects for g_R in comparison to the SM and other NP scenarios. For all the cases, this distinction would be facilitated in higher q^2 bins and for larger values of $|\mathrm{Im}(g_R)|$. Clearly, constraining the branching ratio of $B_c \to \tau\bar{\nu}_\tau$ would be extremely crucial in identifying physics beyond SMEFT. Along with more data for this process, a better understanding of the p_T dependence of the fragmentation function in B_c decay will be needed to put a tighter bound on this branching ratio.

The decay of $\Lambda_b \to \Lambda_c(\Lambda\pi)\tau\bar{\nu}_\tau$ has been recently observed at LHCb. Future runs of High-Luminosity LHC are expected to provide more data in this channel. With enough data, the angular distribution in this channel could allow us to identify the presence of the NP operator O_V^{LR}, which will indicate that SMEFT is not a sufficient EFT description of BSM physics beyond the EW scale. This, in turn, would help us probe the nature of Higgs and the mode of realization of $SU(2)_L \times U(1)_Y$ symmetry above the EW scale.

ACKNOWLEDGMENTS

We would like to thank Rick S. Gupta, Soumen Halder, Gagan B. Mohanty, Arnab Roy, and Tuhin S. Roy for useful discussions. We would also like to thank Ajay Salve and Kapil Ghadiali for technical assistance. This work is supported by the Department of Atomic Energy, Government of India, under Project Identification No. RTI 4002. We acknowledge the use of computational facilities of the Department of Theoretical Physics at Tata Institute of Fundamental Research, Mumbai.

APPENDIX A: HADRONIC AMPLITUDES

As mentioned in Sec. II, Eq. (9), the hadronic amplitudes are nonzero only for the combinations

$$H^{VA}_{\lambda_2,\lambda_3} = H^{V}_{\lambda_2,\lambda_3} - H^{A}_{\lambda_2,\lambda_3}, \tag{A1}$$

$$H^{SP}_{\lambda_2,\lambda_3} = H^{S}_{\lambda_2,\lambda_3} + H^{P}_{\lambda_2,\lambda_3}. \tag{A2}$$

In this section, we provide explicit expressions for these combinations for all λ_2–λ_3 pairs, in terms of the hadronic form factors $F_+, F_\perp, F_0, G_+, G_\perp$, and G_0 [57].

The hadronic amplitudes involving vector currents are shown in the following:

$$\begin{aligned}
H^{VA}_{\frac{1}{2},0} &= F_+(g_L+g_R+1)(m_{\Lambda_b}+m_{\Lambda_c})\sqrt{Q_-/q^2} \\
&\quad - G_+(g_L-g_R+1)(m_{\Lambda_b}-m_{\Lambda_c})\sqrt{Q_+/q^2}, \\
H^{VA}_{\frac{1}{2},1} &= G_\perp(g_L-g_R+1)\sqrt{2Q_+} \\
&\quad - F_\perp(g_L+g_R+1)\sqrt{2Q_-}, \\
H^{VA}_{\frac{1}{2},t} &= F_0(g_L+g_R+1)(m_{\Lambda_b}-m_{\Lambda_c})\sqrt{Q_+/q^2} \\
&\quad - G_0(g_L-g_R+1)(m_{\Lambda_b}+m_{\Lambda_c})\sqrt{Q_-/q^2}, \\
H^{VA}_{-\frac{1}{2},0} &= F_+(g_L+g_R+1)(m_{\Lambda_b}+m_{\Lambda_c})\sqrt{Q_-/q^2} \\
&\quad + G_+(g_L-g_R+1)(m_{\Lambda_b}-m_{\Lambda_c})\sqrt{Q_+/q^2}, \\
H^{VA}_{-\frac{1}{2},-1} &= -F_\perp(g_L+g_R+1)\sqrt{2Q_-} \\
&\quad - G_\perp(g_L-g_R+1)\sqrt{2Q_+}, \\
H^{VA}_{-\frac{1}{2},t} &= F_0(g_L+g_R+1)(m_{\Lambda_b}-m_{\Lambda_c})\sqrt{Q_+/q^2} \\
&\quad + G_0(g_L-g_R+1)(m_{\Lambda_b}+m_{\Lambda_c})\sqrt{Q_-/q^2}.
\end{aligned} \tag{A3}$$

Here $Q_+ = (m_{\Lambda_b} + m_{\Lambda_c})^2 - q^2$ and $Q_- = (m_{\Lambda_b} - m_{\Lambda_c})^2 - q^2$, with q^2 being the total invariant mass squared of the leptons τ and $\bar{\nu}_\tau$. The suffix t indicates the contribution from $s_3 = 0$. The values of hadronic form factors $F_+, F_\perp, F_0, G_+, G_\perp$, and G_0 are as obtained in [49] using the "nominal fit."

The hadronic amplitudes involving scalar currents are

$$H^{SP}_{\frac{1}{2},t} = \frac{F_0 g_S (m_{\Lambda_b} - m_{\Lambda_c})\sqrt{Q_+}}{m_b - m_c} - \frac{G_0 g_P (m_{\Lambda_b} + m_{\Lambda_c})\sqrt{Q_-}}{m_b + m_c},$$
$$H^{SP}_{-\frac{1}{2},t} = \frac{F_0 g_S (m_{\Lambda_b} - m_{\Lambda_c})\sqrt{Q_+}}{m_b - m_c} + \frac{G_0 g_P (m_{\Lambda_b} + m_{\Lambda_c})\sqrt{Q_-}}{m_b + m_c}. \tag{A4}$$

APPENDIX B: EXTRACTING ANGULAR OBSERVABLES

The coefficients of the angular distribution in Eq. (18) can be extracted by a fit to the ten coefficients. Alternatively, they can be extracted by using the orthogonality between different angular functions, using the method of angular moments [64]. We can write the angular distribution in the following form:

$$\frac{1}{d\Gamma/dq^2}\frac{d\Gamma}{dq^2 d\cos\theta_c d\cos\theta_l d\chi} = \sum_i A_i g_i(\cos\theta_c, \cos\theta_l, \chi). \tag{B1}$$

Here A_i are the coefficients of the angular distribution in Eq. (18) and $g_i(\cos\theta_c, \cos\theta_l, \chi)$ are the associated angular functions. We find a "weighting function" $w_i(\cos\theta_c, \cos\theta_l, \chi)$ for each of the g_i such that

$$\int_{-1}^{1} d\cos\theta_l \int_{-1}^{1} d\cos\theta_c \int_0^{2\pi} d\chi \times g_i(\cos\theta_c, \cos\theta_l, \chi) w_j(\cos\theta_c, \cos\theta_l, \chi) = \delta_{ij}, \tag{B2}$$

TABLE V. Weighting functions to extract the coefficients of angular terms from the angular distribution.

Coefficient	Weighting function (w_i)
A_0	$\frac{1}{8\pi} + \frac{5}{32\pi}(1 - 3\cos^2\theta_l)$
A_1	$(\frac{3}{8\pi} + \frac{15}{32\pi}(1 - 3\cos^2\theta_l))\cos\theta_c$
A_2	$\frac{3}{8\pi}\cos\theta_l$
A_3	$\frac{9}{8\pi}\cos\theta_c\cos\theta_l$
A_4	$-\frac{15}{32\pi}(1 - 3\cos^2\theta_l)$
A_5	$-\frac{45}{32\pi}(1 - 3\cos^2\theta_l)\cos\theta_c$
A_6	$\frac{4}{\pi^3}\cos\chi$
A_7	$\frac{4}{\pi^3}\sin\chi$
A_8	$\frac{16}{\pi^3}\cos\chi\cos\theta_l$
A_9	$\frac{16}{\pi^3}\sin\chi\cos\theta_l$

where δ_{ij} is the Kronecker δ function. The value of A_i in a particular q^2 bin can then be determined as

$$A_i(\text{bin}) = \frac{1}{N_{\text{bin}}}\sum_{\text{events}\in\text{bin}} w_i(\cos\theta_c, \cos\theta_l, \chi). \tag{B3}$$

The weighting functions $w_i(\cos\theta_c, \cos\theta_l, \chi)$ are given in Table V. Note that these weighting functions are not unique and may not be experimentally optimal.

APPENDIX C: MAPPING THE ANGULAR DISTRIBUTION ONTO EARLIER LITERATURE

We compare our expressions of the angular distribution with [40], where a discussion about the angular distributions in earlier literature is provided. In [40], the angular distribution of $\Lambda_b \to \Lambda_c(\Lambda\pi)\tau\overline{\nu_\tau}$ decay is given as

$$\begin{aligned} &K(q^2, \cos\theta_l', \cos\theta_c', \chi') \\ &\equiv \frac{8\pi}{3}\frac{1}{d\Gamma/dq^2}\frac{d^4\Gamma}{dq^2 d\cos\theta_l' d\cos\theta_c' d\chi'} \\ &= K_{1ss}\sin^2\theta_l' + K_{1cc}\cos^2\theta_l' + K_{1c}\cos\theta_l' \\ &\quad + (K_{2ss}\sin^2\theta_l' + +K_{2cc}\cos^2\theta_l' + K_{2c}\cos\theta_l')\cos\theta_c' \\ &\quad + (K_{3sc}\sin\theta_l'\cos\theta_l' + K_{3s}\sin\theta_l')\sin\theta_c'\sin\chi' \\ &\quad + (K_{4sc}\sin\theta_l'\cos\theta_l' + K_{4s}\sin\theta_l')\sin\theta_c'\cos\chi'. \end{aligned} \tag{C1}$$

The angles in the above equation are related to the angles defined in Sec. II as

$$\theta_c' \longrightarrow \theta_c, \qquad \theta_l' \longrightarrow \pi - \theta_l, \quad \text{and} \quad \chi' \longrightarrow \chi. \tag{C2}$$

The angular coefficients in Eq. (18) can be mapped onto the coefficients in Eq. (C1) as follows:

$$K_{1ss} \to (8\pi/3)A_0, \qquad K_{1cc} \to (8\pi/3)(A_0 + A_4), \tag{C3}$$

$$K_{1c} \to -(8\pi/3)A_2, \qquad K_{2ss} \to (8\pi/3)A_1, \tag{C4}$$

$$K_{2c} \to -(8\pi/3)A_3, \qquad K_{2cc} \to (8\pi/3)(A_1 + A_5), \tag{C5}$$

$$K_{3sc} \to (8\pi/3)A_9, \qquad K_{3s} \to (8\pi/3)A_7, \tag{C6}$$

$$K_{4sc} \to -(8\pi/3)A_8, \qquad K_{4s} \to (8\pi/3)A_6. \tag{C7}$$

We have chosen the convention for the angles following [58], as it provides a general procedure to calculate angular distribution using helicity amplitudes for many such decays. This convention also matches with [54,56]. The form of our angular terms is similar to that in [42], where the angular distribution is given in term of helicities of Λ and τ.

APPENDIX D: BEYOND-SMEFT EFFECTS IN DIFFERENT q^2 BINS OVER THE g_R PARAMETER SPACE

In Sec. III, we presented our results with the best-fit value of g_R and discussed the possibility of distinguishing it from SM and from the NP scenarios g_L, s_L, and s_R. In this section, we vary g_R over its 2σ-allowed range and indicate those regions for which the distinction from the other scenarios would be theoretically clean in a given q^2 bin. By this criteria, we mean that the theoretical prediction for the given observable in the given q^2 bin has no overlap between the g_R scenario and the other scenarios, even taking into account the theoretical uncertainties. Note that this approach as presented in Fig. 9 is a crude way of recording the separation of bands in Figs. 4–6 and 8 in a binary manner (nonzero overlap or no overlap). It does not necessarily correspond to experimental feasibility of identifying g_R.

The analysis of $\Lambda_b \to \Lambda_c(\to \Lambda\pi)\tau\bar{\nu}_\tau$ in the LHCb experiment [46] is carried out by dividing the data in six q^2 bins, in the range 0–$(m_{\Lambda_b} - m_{\Lambda_c})^2$. The bins (A, B, C, D, E, F) correspond to the q^2 ranges (0–1.83, 1.83–3.67, 3.67–5.5, 5.50–7.33, 7.33–9.17, 9.17–11.13) GeV^2. The first bin cannot have any signal events since $m_\tau^2 = 3.16$ GeV^2, while bin B also does not give any significant number of events [46]. Therefore, we focus only on the four bins C, D, E, and F. Note that the angular analysis performed in the actual experimental analysis may not follow the same q^2 binning scheme as presented in [46]. Our choice of bins is only for the purpose of illustration. Presenting the results in different q^2 bins highlights the fact that the separation of the g_R scenario from the other scenarios may not be possible in all the bins but only in some subsets of them. Note that when clear separation happens in any of the bins, it indicates a signal of physics beyond SMEFT.

For every point in the 2σ-allowed region of g_R in our analysis, we check if the effects of g_R can be distinguishable (i) from SM and g_L and/or (ii) from other NP scenarios, s_L and s_R, in each of these four bins. In Fig. 9, we represent the g_R values that can be distinguishable from both (i) and (ii) by orange color. Those g_R that can be distinguishable from (i) but not from (ii) are denoted by cyan color, while those values that can be distinguishable neither from (i) nor from (ii) are denoted by black. Here, by being distinguishable we mean that the predicted values of the observable in that bin for that particular g_R value do not overlap with the predicted values for the scenarios (i) or (ii). We take into account the 2σ uncertainties due to the hadronic form factors and the polarization asymmetry α_P, as earlier.

Note that the constraints on g_R used in our fit in Sec. III are independent of the sign of $\mathrm{Im}(g_R)$. Therefore, the allowed region of g_R is symmetric with respect to the real axis. We use this fact to show the comparison between the two scenarios $\mathcal{B}(B_c \to \tau\bar{\nu}_\tau) < 30\%$ and $\mathcal{B}(B_c \to \tau\bar{\nu}_\tau) < 10\%$ in a compact manner. We use the upper half of the region (unshaded) to show the constraints when $\mathcal{B}(B_c \to \tau\bar{\nu}_\tau) < 30\%$ and the lower half (shaded) to show the constraints when $\mathcal{B}(B_c \to \tau\bar{\nu}_\tau) < 10\%$. The presence of the corresponding regions reflected about the $\mathrm{Re}(g_R)$ axis is implicit.

Based on the discussion in Sec. III, we focus on the angular observables A_2, A_7 and the ratios $R_{3,1}$, $R_{3,5}$, and $R_{6,8}$, as they are expected to be more suitable in distinguishing g_R from the other scenarios. We note the following:

(i) Using A_7, it may be possible to distinguish g_R from the SM as well as from all the other NP scenarios in most of the allowed 2σ range of g_R.

(ii) With the loose constraint $\mathcal{B}(B_c \to \tau\bar{\nu}_\tau) < 30\%$, we find that the ratios $R_{3,1}$, $R_{3,5}$, and $R_{6,8}$ and the angular observable A_2 may be able to distinguish a large region of g_R from SM and g_L, but would be unable to distinguish it from s_L or s_R. Only a small g_R parameter space can be distinguishable from the effects of s_L and s_R in higher q^2 bins.

(iii) On the other hand, the tighter constraint $\mathcal{B}(B_c \to \tau\bar{\nu}_\tau) < 10\%$ allows the ratios $R_{3,1}$ and $R_{3,5}$ to distinguish large regions in the g_R parameter space from all the other scenarios.

(iv) The power of distinction is typically higher for larger values of $|\mathrm{Im}(g_R)|$.

(v) For all the five observables, the power of distinguishing g_R from the other scenarios appears to be higher at larger q^2.

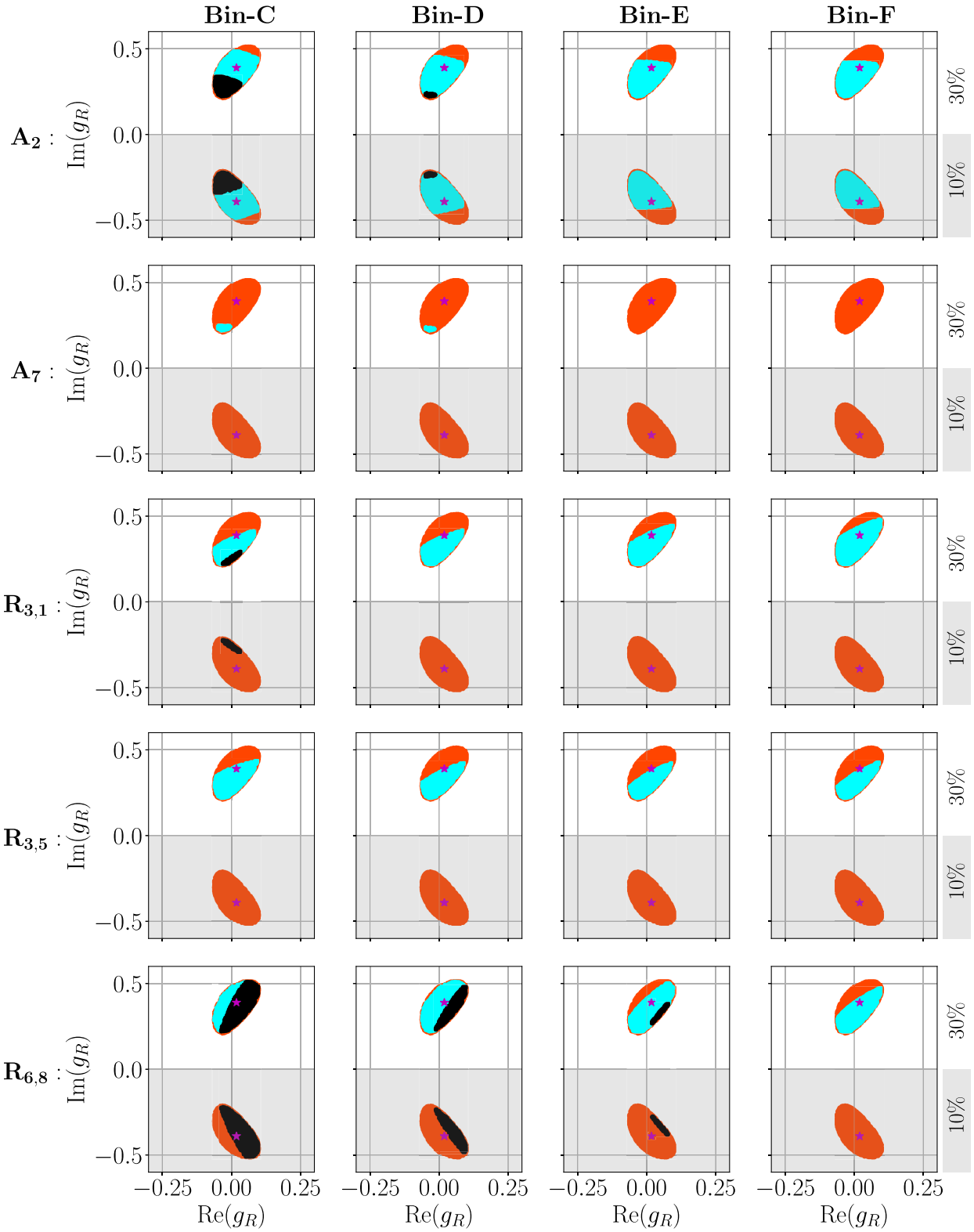

FIG. 9. The 2σ-allowed parameter space of g_R, where the g_R scenario can be distinguished from all the other scenarios $\{\mathrm{SM}, g_L, s_L, s_R\}$ (orange), from only SM and g_L (cyan), and from neither (black). The best-fit value of g_R is denoted by a star. The upper half of each panel (unshaded) corresponds to results for $\mathcal{B}(B_c \to \tau\bar{\nu}_\tau) < 30\%$, while the lower half (shaded) corresponds to $\mathcal{B}(B_c \to \tau\bar{\nu}_\tau) < 10\%$.

[1] W. Buchmuller and D. Wyler, Effective Lagrangian analysis of new interactions and flavor conservation, Nucl. Phys. **B268**, 621 (1986).

[2] B. Grzadkowski, M. Iskrzynski, M. Misiak, and J. Rosiek, Dimension-six terms in the standard model Lagrangian, J. High Energy Phys. 10 (2010) 085.

[3] E. E. Jenkins, A. V. Manohar, and M. Trott, Renormalization group evolution of the standard model dimension six operators I: Formalism and lambda dependence, J. High Energy Phys. 10 (2013) 087.

[4] G. Isidori, F. Wilsch, and D. Wyler, The standard model effective field theory at work, Rev. Mod. Phys. **96**, 015006 (2024).

[5] F. Feruglio, The chiral approach to the electroweak interactions, Int. J. Mod. Phys. A **08**, 4937 (1993).

[6] LHC Higgs Cross Section Working Group, Handbook of LHC Higgs cross sections: 4. Deciphering the nature of the Higgs sector, arXiv:1610.07922.

[7] J. Alison *et al.*, Higgs boson potential at colliders: Status and perspectives, Rev. Phys. **5**, 100045 (2020).

[8] R. Grober *et al.*, Effective field theory descriptions of Higgs boson pair production, Technical Report, CERN, Geneva, 2022.

[9] CMS Collaboration, A portrait of the Higgs boson by the CMS experiment ten years after the discovery, Nature (London) **607**, 60 (2022).

[10] R. Alonso, M. B. Gavela, L. Merlo, S. Rigolin, and J. Yepes, The effective chiral Lagrangian for a light dynamical Higgs Particle, Phys. Lett. B **722**, 330 (2013).

[11] G. Buchalla, O. Catà, and C. Krause, Complete electroweak chiral Lagrangian with a light Higgs at NLO, Nucl. Phys. **B880**, 552 (2014).

[12] A. Pich, I. Rosell, J. Santos, and J. J. Sanz-Cillero, Fingerprints of heavy scales in electroweak effective Lagrangians, J. High Energy Phys. 04 (2017) 012.

[13] T. Cohen, N. Craig, X. Lu, and D. Sutherland, Is SMEFT enough?, J. High Energy Phys. 03 (2021) 237.

[14] *BABAR* Collaboration, Evidence for an excess of $\bar{B} \to D^{(*)}\tau^-\bar{\nu}_\tau$ decays, Phys. Rev. Lett. **109**, 101802 (2012).

[15] *BABAR* Collaboration, Measurement of an excess of $\bar{B} \to D^{(*)}\tau^-\bar{\nu}_\tau$ decays and implications for charged Higgs bosons, Phys. Rev. D **88**, 072012 (2013).

[16] Belle Collaboration, Measurement of the branching ratio of $\bar{B} \to D^{(*)}\tau^-\bar{\nu}_\tau$ relative to $\bar{B} \to D^{(*)}\ell^-\bar{\nu}_\ell$ decays with hadronic tagging at Belle, Phys. Rev. D **92**, 072014 (2015).

[17] LHCb Collaboration, Measurement of the ratio of branching fractions $\mathcal{B}(\bar{B}^0 \to D^{*+}\tau^-\bar{\nu}_\tau)/\mathcal{B}(\bar{B}^0 \to D^{*+}\mu^-\bar{\nu}_\mu)$, Phys. Rev. Lett. **115**, 111803 (2015).

[18] LHCb Collaboration, Measurement of the ratio of branching fractions $\mathcal{B}(B_c^+ \to J/\psi\tau^+\nu_\tau)/\mathcal{B}(B_c^+ \to J/\psi\mu^+\nu_\mu)$, Phys. Rev. Lett. **120**, 121801 (2018).

[19] LHCb Collaboration, Differential branching fractions and isospin asymmetries of $B \to K^{(*)}\mu^+\mu^-$ decays, J. High Energy Phys. 06 (2014) 133.

[20] LHCb Collaboration, Measurement of lepton universality parameters in $B^+ \to K^+\ell^+\ell^-$ and $B^0 \to K^{*0}\ell^+\ell^-$ decays, Phys. Rev. D **108**, 032002 (2023).

[21] LHCb Collaboration, Measurement of form-factor-independent observables in the decay $B^0 \to K^{*0}\mu^+\mu^-$, Phys. Rev. Lett. **111**, 191801 (2013).

[22] S. Descotes-Genon, J. Matias, M. Ramon, and J. Virto, Implications from clean observables for the binned analysis of $B \to K^*\mu^+\mu^-$ at large recoil, J. High Energy Phys. 01 (2013) 048.

[23] S. Descotes-Genon, J. Matias, and J. Virto, Understanding the $B \to K^*\mu^+\mu^-$ anomaly, Phys. Rev. D **88**, 074002 (2013).

[24] E. E. Jenkins, A. V. Manohar, and P. Stoffer, Low-energy effective field theory below the electroweak scale: Operators and matching, J. High Energy Phys. 03 (2018) 016.

[25] J. Aebischer, M. Fael, C. Greub, and J. Virto, B physics beyond the standard model at one loop: Complete renormalization group evolution below the electroweak scale, J. High Energy Phys. 09 (2017) 158.

[26] J. Aebischer *et al.*, WCxf: An exchange format for Wilson coefficients beyond the standard model, Comput. Phys. Commun. **232**, 71 (2018).

[27] D. London and J. Matias, B flavour anomalies: 2021 theoretical status report, Annu. Rev. Nucl. Part. Sci. **72**, 37 (2022).

[28] G. Buchalla, A. J. Buras, and M. E. Lautenbacher, Weak decays beyond leading logarithms, Rev. Mod. Phys. **68**, 1125 (1996).

[29] J. Aebischer, A. Crivellin, M. Fael, and C. Greub, Matching of gauge invariant dimension-six operators for $b \to s$ and $b \to c$ transitions, J. High Energy Phys. 05 (2016) 037.

[30] E. E. Jenkins, A. V. Manohar, and P. Stoffer, Low-energy effective field theory below the electroweak scale: Anomalous dimensions, J. High Energy Phys. 01 (2018) 084.

[31] R. Alonso, B. Grinstein, and J. Martin Camalich, $SU(2) \times U(1)$ gauge invariance and the shape of new physics in rare B decays, Phys. Rev. Lett. **113**, 241802 (2014).

[32] O. Catà and M. Jung, Signatures of a nonstandard Higgs boson from flavor physics, Phys. Rev. D **92**, 055018 (2015).

[33] C. P. Burgess, S. Hamoudou, J. Kumar, and D. London, Beyond the standard model effective field theory with $B \to c\tau^-\bar{\nu}$, Phys. Rev. D **105**, 073008 (2022).

[34] M. Jacob and G. C. Wick, On the general theory of collisions for particles with spin, Ann. Phys. (N.Y.) **7**, 404 (1959).

[35] I. Banta, T. Cohen, N. Craig, X. Lu, and D. Sutherland, Non-decoupling new particles, J. High Energy Phys. 02 (2022) 029.

[36] G. Buchalla and O. Cata, Effective theory of a dynamically broken electroweak standard model at NLO, J. High Energy Phys. 07 (2012) 101.

[37] V. Cirigliano, J. Jenkins, and M. Gonzalez-Alonso, Semileptonic decays of light quarks beyond the standard model, Nucl. Phys. **B830**, 95 (2010).

[38] M. Blanke, A. Crivellin, S. de Boer, M. Moscati, U. Nierste, I. Nišandžić, and T. Kitahara, Impact of polarization observables and $B_c \to \tau\nu$ on new physics explanations of the $b \to c\tau\nu$ anomaly, Phys. Rev. D **99**, 075006 (2019).

[39] M. Blanke, A. Crivellin, T. Kitahara, M. Moscati, U. Nierste, and I. Nišandžić, Addendum to "Impact of polarization observables and $B_c \to \tau\nu$ on new physics explanations of the $b \to c\tau\nu$ anomaly, Phys. Rev. D **100**, 035035 (2019).

[40] P. Böer, A. Kokulu, J.-N. Toelstede, and D. van Dyk, Angular analysis of $\Lambda_b \to \Lambda_c(\to \Lambda\pi)\ell\bar{\nu}$, J. High Energy Phys. 12 (2019) 082.

[41] Q.-Y. Hu, X.-Q. Li, and Y.-D. Yang, $b \to c\tau\nu$ transitions in the standard model effective field theory, Eur. Phys. J. C **79**, 264 (2019).

[42] D. Bečirević and F. Jaffredo, Looking for the effects of new physics in the $\Lambda_b \longrightarrow \Lambda_c(\to \Lambda\pi)\ell\nu$ decay mode, arXiv: 2209.13409.

[43] A. Ray, S. Sahoo, and R. Mohanta, Model independent analysis of $B^* \to P\ell\bar{\nu}_\ell$ decay processes, Eur. Phys. J. C **79**, 670 (2019).

[44] Z.-R. Huang, E. Kou, C.-D. Lü, and R.-Y. Tang, Unbinned angular analysis of $B \to D^*(D\pi)\ell\nu_\ell$ and C_{V_R}, in *30th International Symposium on Lepton Photon Interactions at High Energies* (2022), 4, arXiv:2204.06814.

[45] Q.-Y. Hu, X.-Q. Li, Y.-D. Yang, and D.-H. Zheng, The measurable angular distribution of $\Lambda_b^0 \to \Lambda_c^+(\to \Lambda^0\pi^+) \times \tau^-(\to \pi^- v_\tau)\bar{\nu}_\tau$ decay, J. High Energy Phys. 02 (2021) 183.

[46] LHCb Collaboration, Observation of the decay $\Lambda_b^0 \to \Lambda_c^+\tau^-\bar{\nu}_\tau$, Phys. Rev. Lett. **128**, 191803 (2022).

[47] S. Shivashankara, W. Wu, and A. Datta, $\Lambda_b \to \Lambda_c\tau\bar{\nu}_\tau$ decay in the standard model and with new physics, Phys. Rev. D **91**, 115003 (2015).

[48] R. Dutta, $\Lambda_b \to (\Lambda_c, p)\tau\nu$ decays within standard model and beyond, Phys. Rev. D **93**, 054003 (2016).

[49] W. Detmold, C. Lehner, and S. Meinel, $\Lambda_b \to p\ell^-\bar{\nu}_\ell$ and $\Lambda_b \to \Lambda_c\ell^-\bar{\nu}_\ell$ form factors from lattice QCD with relativistic heavy quarks, Phys. Rev. D **92**, 034503 (2015).

[50] X.-Q. Li, Y.-D. Yang, and X. Zhang, $\Lambda_b \to \Lambda_c\tau\bar{\nu}_\tau$ decay in scalar and vector leptoquark scenarios, J. High Energy Phys. 02 (2017) 068.

[51] E. Di Salvo, F. Fontanelli, and Z. J. Ajaltouni, Detailed study of the decay $\Lambda_b \to \Lambda_c\tau\bar{\nu}_\tau$, Int. J. Mod. Phys. A **33**, 1850169 (2018).

[52] A. Ray, S. Sahoo, and R. Mohanta, Probing new physics in semileptonic Λ_b decays, Phys. Rev. D **99**, 015015 (2019).

[53] N. Penalva, E. Hernández, and J. Nieves, Further tests of lepton flavour universality from the charged lepton energy distribution in $b \to c$ semileptonic decays: The case of $\Lambda_b \to \Lambda_c\ell\bar{\nu}_\ell$, Phys. Rev. D **100**, 113007 (2019).

[54] T. Gutsche, M. A. Ivanov, J. G. Korner, V. E. Lyubovitskij, and P. Santorelli, Semileptonic decays $\Lambda_c^+ \to \Lambda\ell^+\nu_\ell(\ell = e, \mu)$ in the covariant quark model and comparison with the new absolute branching fraction measurements of Belle and BESIII, Phys. Rev. D **93**, 034008 (2016).

[55] M. Ferrillo, A. Mathad, P. Owen, and N. Serra, Probing effects of new physics in $\Lambda_b^0 \to \Lambda_c^+\mu^-\bar{\nu}_\mu$ decays, J. High Energy Phys. 12 (2019) 148.

[56] X.-L. Mu, Y. Li, Z.-T. Zou, and B. Zhu, Investigation of effects of new physics in $\Lambda_b \to \Lambda_c\tau\bar{\nu}_\tau$ decay, Phys. Rev. D **100**, 113004 (2019).

[57] A. Datta, S. Kamali, S. Meinel, and A. Rashed, Phenomenology of $\Lambda_b \to \Lambda_c\tau\bar{\nu}_\tau$ using lattice QCD calculations, J. High Energy Phys. 08 (2017) 131.

[58] R. Kutschke, An angular distribution cookbook (to be published).

[59] J. D. Richman, An experimenter's guide to the helicity formalism, CALT-68-1148 (1984).

[60] A. Kadeer, J. G. Korner, and U. Moosbrugger, Helicity analysis of semileptonic hyperon decays including lepton mass effects, Eur. Phys. J. C **59**, 27 (2009).

[61] LHCb Collaboration, Test of lepton flavor universality by the measurement of the $B^0 \to D^{*-}\tau^+\nu_\tau$ branching fraction using three-prong τ decays, Phys. Rev. D **97**, 072013 (2018).

[62] Particle Data Group, Review of particle physics, Prog. Theor. Exp. Phys. **2022**, 083C01 (2022).

[63] Q. Chang, J. Zhu, N. Wang, and R.-M. Wang, Probing the effects of new physics in $\bar{B}^* \to P\ell\bar{\nu}_\ell$ decays, Adv. High Energy Phys. **2018**, 7231354 (2018).

[64] A. S. Dighe, I. Dunietz, and R. Fleischer, Extracting CKM phases and $B_s - \bar{B}_s$ mixing parameters from angular distributions of nonleptonic B decays, Eur. Phys. J. C **6**, 647 (1999).

[65] S. Iguro, T. Kitahara, and R. Watanabe, Global fit to $b \to c\tau\nu$ anomalies 2022 mid-autumn, arXiv:2210.10751.

[66] Heavy Flavor Averaging Group (HFLAV Collaboration), Semileptonic B Decays (2023), https://hflav-eos.web.cern.ch/hflav-eos/semi/summer23/html/RDsDsstar/RDRDs.html.

[67] Belle Collaboration, Measurement of $\mathcal{R}(D)$ and $\mathcal{R}(D^*)$ with a semileptonic tagging method, arXiv:1904.08794.

[68] Y. Amhis *et al.*, Averages of b-hadron, c-hadron, and τ-lepton properties as of 2021, Phys. Rev. D **107**, 052008 (2023).

[69] MILC Collaboration, B → D$\ell\nu$ form factors at nonzero recoil and —V_{cb}— from 2 + 1-flavor lattice QCD, Phys. Rev. D **92**, 034506 (2015).

[70] HPQCD Collaboration, $B \to Dl\nu$ form factors at nonzero recoil and extraction of $|V_{cb}|$, Phys. Rev. D **92**, 054510 (2015).

[71] S. Aoki *et al.*, Review of lattice results concerning low-energy particle physics, Eur. Phys. J. C **77**, 112 (2017).

[72] D. Bigi and P. Gambino, Revisiting $B \to D\ell\nu$, Phys. Rev. D **94**, 094008 (2016).

[73] Belle Collaboration, Measurement of the branching ratio of $\bar{B}^0 \to D^{*+}\tau^-\bar{\nu}_\tau$ relative to $\bar{B}^0 \to D^{*+}\ell^-\bar{\nu}_\ell$ decays with a semileptonic tagging method, Phys. Rev. D **94**, 072007 (2016).

[74] LHCb Collaboration, Measurement of the ratio of the $B^0 \to D^{*-}\tau^+\nu_\tau$ and $B^0 \to D^{*-}\mu^+\nu_\mu$ branching fractions using three-prong τ-lepton decays, Phys. Rev. Lett. **120**, 171802 (2018).

[75] Belle Collaboration, Measurement of the τ lepton polarization and $R(D^*)$ in the decay $\bar{B} \to D^*\tau^-\bar{\nu}_\tau$, Phys. Rev. Lett. **118**, 211801 (2017).

[76] Belle Collaboration, Measurement of the τ lepton polarization and $R(D^*)$ in the decay $\bar{B} \to D^*\tau^-\bar{\nu}_\tau$ with one-prong hadronic τ decays at Belle, Phys. Rev. D **97**, 012004 (2018).

[77] F. U. Bernlochner, Z. Ligeti, M. Papucci, and D. J. Robinson, Combined analysis of semileptonic B decays to D and D^*: $R(D^{(*)})$, $|V_{cb}|$, and new physics, Phys. Rev. D **95**, 115008 (2017).

[78] S. Jaiswal, S. Nandi, and S. K. Patra, Extraction of $|V_{cb}|$ from $B \to D^{(*)}\ell\nu_\ell$ and the standard model predictions of $R(D^{(*)})$, J. High Energy Phys. 12 (2017) 060.

[79] S. Fajfer, J. F. Kamenik, and I. Nisandzic, On the $B \to D^*\tau\bar{\nu}_\tau$ sensitivity to new physics, Phys. Rev. D **85**, 094025 (2012).

[80] T. D. Cohen, H. Lamm, and R. F. Lebed, Model-independent bounds on $R(J/\psi)$, J. High Energy Phys. 09 (2018) 168.

[81] LATTICE-HPQCD Collaboration, $R(J/\psi)$ and $B_c^- \to J/\psi \ell^- \bar{\nu}_\ell$ lepton flavor universality violating observables from lattice QCD, Phys. Rev. Lett. **125**, 222003 (2020).

[82] M. Tanaka and R. Watanabe, New physics in the weak interaction of $\bar{B} \to D^{(*)}\tau\bar{\nu}$, Phys. Rev. D **87**, 034028 (2013).

[83] Belle Collaboration, Measurement of the D^{*-} polarization in the decay $B^0 \to D^{*-}\tau^+\nu_\tau$, in *10th International Workshop on the CKM Unitarity Triangle* (2019), arXiv:1903.03102.

[84] A. K. Alok, D. Kumar, S. Kumbhakar, and S. U. Sankar, D^* polarization as a probe to discriminate new physics in $\bar{B} \to D^*\tau\bar{\nu}$, Phys. Rev. D **95**, 115038 (2017).

[85] H. Dembinski and P. Ongmongkolkul *et al.*, The latest iminuit release scikit-hep/iminuit (2020), 10.5281/zenodo.3949207.

[86] R. Alonso, B. Grinstein, and J. Martin Camalich, Lifetime of B_c^- constrains explanations for anomalies in $B \to D^{(*)}\tau\nu$, Phys. Rev. Lett. **118**, 081802 (2017).

[87] A. G. Akeroyd and C.-H. Chen, Constraint on the branching ratio of $B_c \to \tau\bar{\nu}$ from LEP1 and consequences for $R(D^{(*)})$ anomaly, Phys. Rev. D **96**, 075011 (2017).

[88] D. Bardhan and D. Ghosh, B -meson charged current anomalies: The post-Moriond 2019 status, Phys. Rev. D **100**, 011701 (2019).

[89] N. Das, A. Adhikary, and R. Dutta, Revisiting $b \to c\tau\nu$ anomalies with charged Higgs boson, arXiv:2305.17766.

[90] M. Arslan, T. Yasmeen, S. Shafaq, I. Ahmed, and M. J. Aslam, Analysis of $b \to c\tau\bar{\nu}_\tau$ anomalies using weak effective Hamiltonian with complex couplings, arXiv:2309.09929.

[91] T. Zheng, J. Xu, L. Cao, D. Yu, W. Wang, S. Prell, Y.-K. E. Cheung, and M. Ruan, Analysis of $B_c \to \tau\nu_\tau$ at CEPC, Chin. Phys. C **45**, 023001 (2021).

[92] Y. Amhis, M. Hartmann, C. Helsens, D. Hill, and O. Sumensari, Prospects for $B_c^+ \to \tau^+\nu_\tau$ at FCC-ee, J. High Energy Phys. 12 (2021) 133.